COMPUTATIONAL MODELS OF FLUID FLOW, STRUCTURAL VIBRATION AND FLUID-STRUCTURE INTERACTIONS OF HUMAN PHONATION

A Thesis

Submitted to the Faculty

of

Purdue University

by

Douglas Dwight Cook

In Partial Fulfillment of the

Requirements for the Degree

of

Master of Science in Mechanical Engineering

December 2005

ACKNOWLEDGEMENTS

I would like to thank my advisor, Professor Luc Mongeau, my Advisory Committee members: Dr. Steven Frankel, and Dr. Anil Bajaj, and my Examination Committee Members: Dr. Arvind Raman, Dr. Mahalakshmi Sivasankar, and Dr. Thomas Siegmund. Valuable guidance and support was provided by Dr. Scott Thomson. I gratefully acknowledge the financial support of the National Institute on Deafness and Other Communication Disorders (Grant # R01 DC005788). Finally, I acknowledge the profound support of my wife, TaraLee, who has encouraged and supported my graduate education.

TABLE OF CONTENTS

Page

Page

LIST OF TABLES

LIST OF FIGURES

NOMENCLATURE

A	Area
$\mathbf{A}$	Symmetric matrix
A_{ij}	Coefficient
AR	Aspect Ratio
B	Bulk modulus
$\mathbf{B}$	Symmetric matrix
B_{mn}	Coefficient
c	Damping factor
C	Orifice discharge coefficient
[C]	Matrix of elastic coefficients
D	Depth
E	Young's modulus
E_i	Young's modulus in the *i* direction
E_{long}	Young's modulus in the longitudinal direction
E_{trans}	Young's modulus in the transverse plane
F_{fl}	Net fluid force
G	Orifice gap
G_0	Initial distance between the upper and orifice walls
$G_{\max}$	Maximum gap distance
$G_{\min}$	Minimum gap distance
H_O	Orifice height
I_1	Internal strain energy

I_2	Kinetic energy
K	Adiabatic bulk modulus
k	Spring constant
L	Length
L_O	Orifice lLength
m	Mass
MF	Magnification factor
n	Isotropy ratio
P	Pressure
P_i	Instantaneous power attributed to the i component
$\mathbf{Q}$	Stiffness matrix
R	Gas Constant
$\mathbf{R}$	Mass matrix
T	Period of oscillation
T	Temperature
T	Thickness
t	Time
$\mathbf{u}$	Velocity vector
V	Volume
$\dot{V}$	Volumetric flow rate
$\mathbf{v}$	Vector of coefficients
W_{damp}	Net work done by the damper element
W_{fl}	Net work done by the fluid
W_{sp}	Net work done by the spring
$\mathbf{x}$	Eigenvector
x	Displacement in the x-direction
$\dot{x}$	Velocity in the x-direction
$\ddot{x}$	Acceleration in the x-direction
y	Displacement in the y-direction
z	Displacement in the z-direction

Δt	Timestep
γ	Rratio of constant-pressure specific heat to constant-volume specific heat
γ_{ij}	Shear strain in the *ij* plane
$[\varepsilon]$	Vector of strains
ε_{ii}	Normal strain in the *i* direction
ζ	Displacement function in the z-direction
λ	Eigenvalue
μ	Viscosity
μ'	Longitudinal shear modulus
μ_{trans}	Transverse shear modulus
μ_{xy}	Shear modulus in the xy plane
ξ	The x direction displacement function
π	Pi, the ratio of a circle's circumference to diameter
Π	Total potential energy of a continuum
ρ	Density
$[\sigma]$	Vector of stresses
σ_{ii}	Stress normal to the *i* direction
σ_{yy}	Stresses normal to the xz plane
τ_{ij}	Shear stress on the *i* face in the *j* direction.
υ'	Longitudinal Poisson's ratio
υ_{ij}	Poisson's ratio of contraction in the *i* direction to strain in the *j* direction
υ_{long}	Longitudinal Poisson's ratio
υ_{trans}	Transverse Poisson's ratio
ψ	Included Angle
ψ	Displacement function in the y-direction
ω	Angular frequency

ABSTRACT

Cook, Douglas Dwight, M.S.M.E., Purdue University, December 2005. Computational Models of Fluid Flow, Fluid Structure-Interactions and Structural Vibration of Human Phonation. Major Professor, Dr. Luc Mongeau, School of Mechanical Engineering.

The purpose of this study was to characterize mechanisms which contribute to human phonation through the use of structural, fluid, and fluid-structure interaction numerical models. The flow of air through an orifice representative of the glottis was simulated using a finite element Navier-Stokes solver. The motion of the orifice was imposed through moving boundary conditions. Simulation results were found to be in good qualitative agreement with experimental data from a parallel study. Discrepancies in velocity amplitude were due to the incomplete matching of boundary conditions between the model and the experiment. A lumped single degree-of-freedom model of the vocal folds was coupled to a viscous, two-dimensional Navier-Stokes computational fluid domain in order to investigate viscous flow effects on reduced order models. The model geometry was representative of the vocal fold orifice profile with included angles ranging from -10° to 20° in 5° increments and pressure differentials ranging from 100 to 3000 Pa. An energy transfer analysis of the coupled system was performed. Self-oscillation of this model was not observed for any configuration. These results suggest that the presence of viscous effects, flow separation, and other flow effects are not sufficient to induce self-oscillation of a single mass model with a fixed orifice profile. This supports the hypothesis that structural vibrations involving a change in orifice shape are essential to self-oscillation. Modal analysis was used to examine the structural characteristics of a continuum vocal fold structure. The Ritz and finite element methods were used. A geometric sensitivity study was performed in which the major dimensions of the vocal fold model were independently varied. The vibratory properties of the model were determined to be most sensitive to changes in the length of the model. Further results indicated that the continuum model is an inherently three-dimensional structure. The vibratory characteristics of this model were significantly influenced by out of plane shear and normal stresses which are ignored by two-dimensional planar strain models. The human vocal folds may be similarly influenced these stresses.

1. INTRODUCTION AND BACKGROUND

This chapter provides an introduction to the location, function, and structure of the human larynx. A description of the mechanics of phonation is given. The motivation and objectives of this study are stated.

1.1 Basic Medical Terminology and Conventions

A coordinate system relative to the human body is used in this study. The coordinate directions x,y, and z, are shown in Figure 1.1. The positive y-direction is referred to as "anterior" by medical experts. The opposite direction is referred to as "posterior". Likewise, the positive and negative z-directions are referred to as "superior" and "inferior". Due to symmetry of the human body about the mid-sagittal plane, the positive and negative x-directions are not distinguished explicitly. Instead, "lateral" always indicates distance from the mid-sagittal plane, regardless of the positive or negative x-direction as shown in Figure 1.1.

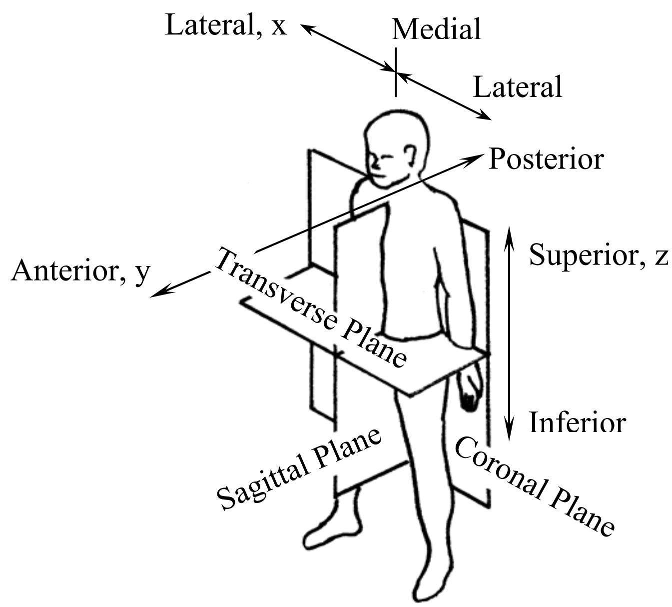

Figure 1.1: Coordinate system and medical terminology (adapted from NASA *Man-Systems Integration Standards*, 1995).

1.2 The Human Larynx

The human larynx is located in the upper region of the airway between the trachea and the pharynx. It extends from the base of the tongue to the trachea, and can often be seen as a projection of the neck, sometimes referred to as the “Adam’s apple”. The larynx is composed of cartelagenous structures, muscles, ligaments and soft tissue layers. The location of the larynx is shown in Figures 1.2 and 1.3.

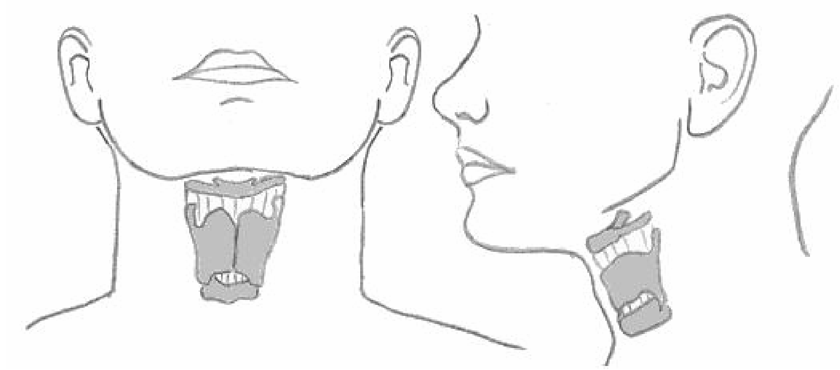

Figure 1.2: Location of the larynx relative to exterior human features (adapted from Larsen, 2002).

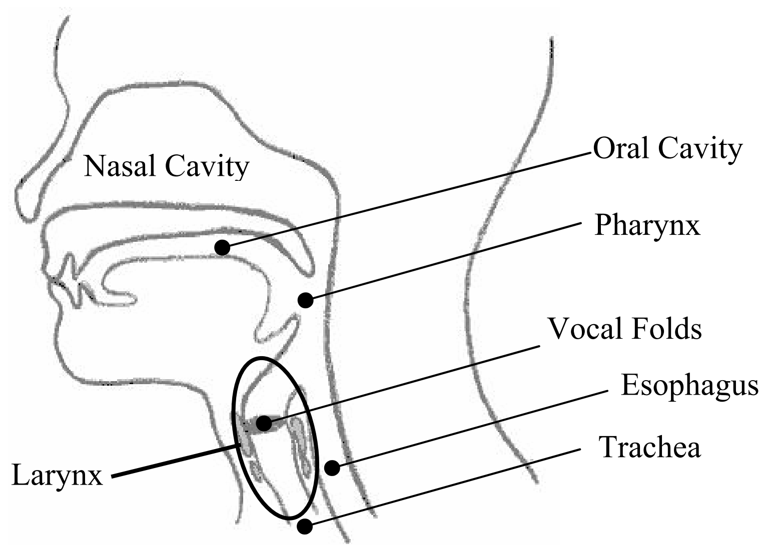

Figure 1.3: Mid-sagittal view of the human larynx and surrounding anatomical features (adapted from Larsen, 2002).

During ingestion, liquids or solids pass through the mouth, pharynx and esophagus into the digestive tract. Inhalation is the passage of air through the nasal and/or oral cavities, pharynx, larynx, and trachea to the lungs. Because of its location, the larynx plays a key role in several important biological functions such as inhalation, ingestion, coughing, vomiting and phonation. This study is focused on phonation, which is the use of the larynx to generate voiced sounds.

1.3 Phonation

Within the larynx are two tissue formations called the vocal folds (also commonly referred to as vocal chords). A coronal cross-section of the larynx is shown in Figure 1.4 in which the vocal folds can be seen as protrusions within the larynx.

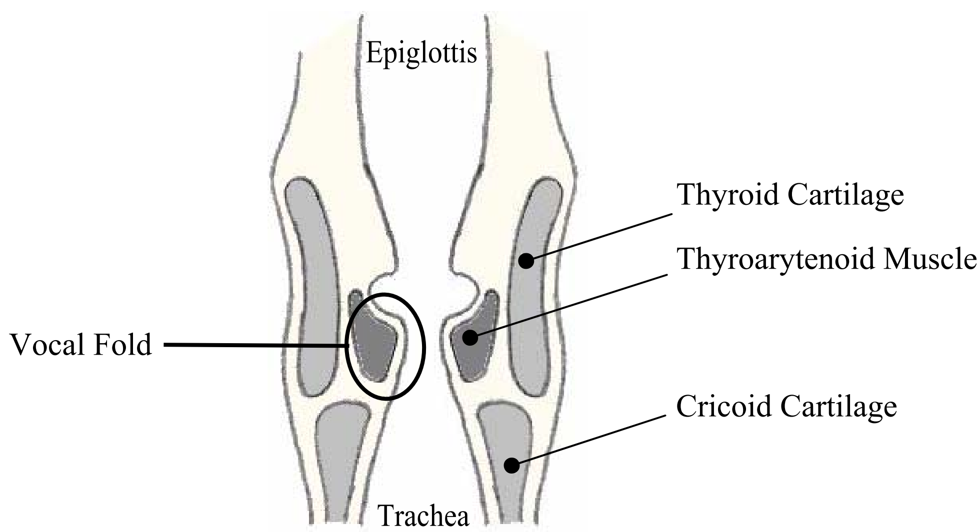

Figure 1.4: Coronal section of the larynx (adapted from Gray, 1918).

The vocal folds are the primary organs of phonation. Each vocal fold is composed of four tissue structures: the epithelium, a thin membrane, the lamina propria, a soft layer composed of collagen and elastin, the vocal ligament, and the thyroarytenoid muscle.

The epithelium and lamina propria together form what is commonly referred to as the "cover" as these two layers form a limp covering for the much stiffer "body" which is composed of the thyroarytenoid muscle and vocal ligament. These four tissue structures are illustrated and identified in Figure 1.5.

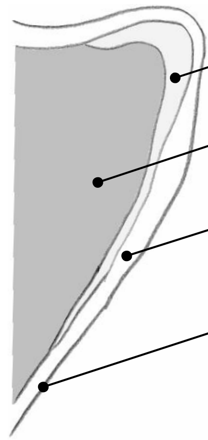

Figure 1.5: The layers of the vocal fold, coronal cross-section diagram (adapted from Hirano and Sato, 1993).

Normal human development results in two vocal folds located on opposite sides of the larynx as shown in Figure 1.4. The vocal folds are generally very similar to each other in size and geometry, resulting in a nearly symmetric airway. The space between the two vocal folds is referred to as the glottis.

At rest and during inhalation the vocal folds are opened to allow air flow to the lungs. Prior to phonation, the vocal folds are brought together as muscles connected to cartilagenous levers contract. This process is known as adduction. The reverse process (the opening of the glottis) is known as abduction. The configuration of the vocal folds during abduction and adduction are shown in Figure 1.6.

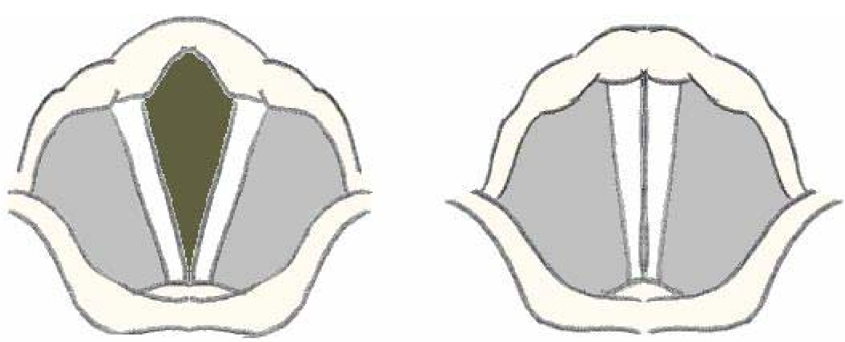

a) (b)

Figure 1.6: View of the vocal folds as seen from the pharynx (adapted from Larsen, 2002): (a) abduction of the vocal folds; (b) adduction of the vocal folds.

Following adduction, positive lung pressure and abdominal muscles are used to produce a net pressure difference between the subglottal and supraglottal regions. When this pressure is sufficiently large to cause deflection of the vocal folds, air is allowed to pass through the larynx. Instability between the aerodynamic and structural forces then induces vocal fold motion. Steady vibration occurs as the system enters into a stable limit cycle. Under these conditions, sustained oscillations of the vocal folds, collisions between the folds, turbulence and compressible flow effects produce a complex acoustic signal. This signal is modified by the vocal tract to become the human voice. The fundamental frequency of normal phonation is usually 90 - 130 Hz for the adult male, 200-250 Hz for the adult female.

Common voice disorders involve paralysis of one or both vocal folds, the presence of polyps, nodules or other benign growths, scarring, misuse or abuse of the vocal folds, or trauma caused by surgery or accidental injury. These pathological conditions result in poor voice quality or the inability to phonate. The most common are benign growths. However, the surgical removal of such growths can produce additional obstacles to proper phonation.

It is estimated that 28 million US workers are adversely affected by some kind of voice disorder (Verdolini and Ramig, 2001). The percentage is much higher among those who rely heavily upon their voice such as teachers, performers, and public speakers. Smith, *et al*. (1997) found that as many as 20% of elementary school teachers had at one time missed school due to a voice disorder. Research also suggests that students learn less effectively when taught by an individual suffering from a voice disorder.

1.4 Research Objectives

The purpose of this study was to identify and quantify mechanisms which contribute to self-oscillation of the human vocal folds. Phonation involves fluid flow, structural vibrations, and fluid-structure interactions. Each of these aspects was addressed within this study.

The first objective was to determine the ability of a computational fluid model to accurately predict dynamic fluid flow representative of human phonation. A commercially available finite element program was used to create a representation of flow through an orifice similar in geometry to the glottis. The motion of the orifice was imposed upon the fluid. This fluid flow behavior predicted by this model was compared to the fluid flow through a synthetic vocal fold model of similar geometry. Comparisons were made between predicted and measured fluid flow fields in order to verify the accuracy of the computational fluid model.

The second objective was to investigate the influence of viscous Navier-Stokes flow on self-oscillation of a lumped mass model. The computational fluid model mentioned above was coupled to a spring-mass-damper structural model of the vocal folds. The profile of the rigid mass was representative of the human vocal folds. In order to eliminate other factors which might contribute to self-oscillation, the flow was assumed to be incompressible and no collisions were allowed. Thus, the spring-mass-damper system was affected only by Navier-Stokes viscous incompressible flow. The ability of this system to exhibit self-oscillation was analyzed.

The final objective was to investigate the structural characteristics of the vocal fold structure. Modal analysis was used to perform a geometric sensitivity analysis of an idealized transversely isotropic continuum model of the vocal folds. The length, width, and thickness of the model were varied independently to determine the structure's sensitivity to these parameters. Modal analysis was used as a descriptive tool to better understand the structural characteristics of the model.

The remainder of the thesis is organized as follows. Chapter Two provides a review of the scientific literature on the subjects and topics investigated. Chapter Three presents the research methods which were utilized. Chapter Four presents fluid flow simulation results. The dynamic behavior of a single degree-of-freedom model of the human vocal folds is analyzed in Chapter Five. Chapter Six presents the results of a modal analysis study in which the vocal fold structure is observed to be inherently three-dimensional. Finally, the work is summarized, conclusions are stated and suggestions for future research are made in Chapter Seven.

2. LITERATURE REVIEW

The complexity and inaccessibility of the human larynx poses many obstacles to detailed studies of human phonation. Nevertheless, the basic understanding of human phonation has progressed in recent years through the use of continuously improving experimental and analytical research techniques. Experiments have been performed *in vivo* on human and canine subjects, *post mortem* on canine subjects, and *in vitro* using synthetic physical models. Mathematical models and analytical techniques have also been employed to investigate the behavior of the human vocal folds. This chapter presents an overview of previous experimental and analytical studies.

2.1 Experimental Studies

2.1.1. Geometric Information

One important requirement for phonation research is a clear understanding of the geometry of the human larynx. Various methods have been employed to obtain this information. These have included dissection, imaging by computed tomography (CT), magnetic resonance imaging (MRI), molding techniques, and plastination.

Scherer *et al.* (2001b) have used CT images of the vocal folds taken at different coronal planes to define a composite vocal fold geometry which was described using mathematical functions. This idealized geometry has been designated M5, and is referred to as such in this document. Recent studies utilizing MRI images (Selbie *et al.*, 2002) have supplied very detailed geometrical descriptions of the larynx cartilages. Quick-frozen canine larynges were used by Tayama *et al.* (2002) to obtain accurate values for vocal fold length and thickness. A wax molding technique was developed by Berry *et al.* (2001) in which polynomial approximations of the vocal fold geometry were produced. A quick-setting dental plaster was used by Sidlof *et al.* (2004) to obtain detailed casts of excised larynges. A mold was created following the casting procedure. A digital three-dimensional representation of the resulting model was obtained using a bridge-type coordinate measuring machine to produce highly detailed geometrical data.

2.1.2. Vocal Fold Tissue Properties

Many studies have been performed to measure and describe the mechanical properties of the human vocal folds. Such properties are difficult to determine due to variability among individuals, variation of tissue properties over time, and the difficulty of obtaining tissue samples via consistent harvesting procedures.

Although the properties of vocal fold tissue are anisotropic, most studies have focused only on measurements of the tissue properties in the anterior-posterior direction. Very little information is available for the transverse (medial-lateral) properties of vocal fold tissue. Min *et al.* (1995) measured axial stress-strain relations for human ligament samples. Stress-strain relations in the direction of muscle fibers were measured by Alipour-Haghighi and Titze (1991) using canine thyroarytenoid muscle samples. In both studies, strain increased non-linearly as a function of strain. Chan and Titze (1999) utilized a parallel-plate rotational rheometer to measure the shear deformation and structural damping characteristics of human vocal fold mucosa samples. Zhang *et al.* (in press) have investigated the stress-strain relationship of the mucosal layer, which also exhibited similar non-linear characteristics. In these studies, a large variation in tissue properties was observed between samples. This variation was observed to be as large as one order of magnitude (Chan and Titze, 1991). A parametric variation of the tissue properties over a wide range was proposed by Berry and Titze (1996) as an alternative to the use of averaged values.

2.1.3. Observations of Self-Oscillating Larynges

Valuable information may be gained by direct observation of vocal fold vibration. Baer (1975), Jiang and Titze (1993) and Berry *et al.* (2001) have conducted experiments which utilized excised canine larynges. In all cases, a flow supply was used to induce oscillation of the canine vocal folds. The resulting vibration was studied using various techniques. Baer (1975) tracked three vocal fold flesh points using stroboscopy to obtain eliptical trajectories of motion. Jiang and Titze (1993) increased the number of flesh points to nine and utilized a hemi-larynx configuration to view the medial surface vibration of the vocal folds. Empirical eigenfunctions were obtained by tracking the motion of micro sutures located on the surface of the vocal folds (Berry *et al.*, 2001). This study noted that the superposition of the two primary eigenfunctions accounted for 98% of the vocal folds' total vibrational energy.

Techniques have also been developed for the observation of human vocal folds *in vivo*. These include high-speed imaging, stroboscopy, and kymography. These methods utilize a laryngoscope to provide optical access to the larynx. The laryngoscope, along with stroboscopy, are used extensively by speech therapists and physicians for the examination, diagnosis, and treatment of patients (Hirano and Bless, 1993).

Kymography has been developed by Svec and Schutte (1996) as an alternative to stroboscopy. This method has the advantage of providing a time/displacement representation of vocal fold vibration as opposed to the discrete aliased images obtained via stroboscopy. Irregularities in motion which are not apparent in stroboscopy may be captured by kymography (Neubauer, 2001).

Svec *et al.* (2000) used kymography to obtain the first *in vivo* measurements of the resonance properties of the human vocal folds. The vocal folds were excited using a small shaker placed externally against the larynx. A frequency sweep was initiated while the motion of the vocal folds was captured via kymography. The vibration amplitude of the vocal folds was then plotted as a function of the excitation frequency. Distinct resonance frequencies were observed at 114, 171 and 241 Hz.

2.1.4. Experiments Involving Synthetic Physical Models

There are many difficulties associated with the use of excised larynges, including rapid deterioration of the excised specimen, and inconsistent harvesting and storage techniques. Synthetic physical models have been developed as an alternative to excised larynges. While synthetic models do not accurately reproduce the properties of the actual vocal folds, their use allows more precise control of experimental conditions. Accurate, repeatable measurements may be made using synthetic models. Thus, synthetic models may be used to investigate the basic mechanisms which cause self-oscillation.

Scherer *et al.* (2001b, 2002) studied the intraglottal pressure distributions of symmetric and asymmetric geometric profiles using rigid models of the vocal folds in a wind tunnel. Results suggested that an oblique glottis configuration could lead to desynchronization of vocal fold oscillation. Scherer (in press) has also investigated the influence of inferior and superior vocal fold surface angles on the pressure profile within the glottis. Results indicated that for typical angles the pressure distribution within the glottis is relatively independent of inferior and superior surface angle.

One common assumption used in creating rigid models of human phonation is that the flow through a static rigid model is identical to the instantaneous flow through a geometrically similar dynamic model. This is referred to as the quasi-steady approximation. Zhang *et al.* (2002) evaluated the quasi-steady approximation for the sound generation of pulsating jets within a tube. A glottis-shaped nozzle was subjected to pulsatile flow in which the Reynolds numbers and oscillation frequencies were representative of human phonation. The quasi-steady approximation was found to be valid for frequencies ranging from 70 – 120 Hz.

Thomson (2004) created a self-oscillating synthetic model using a soft silicone rubber compound which was observed to oscillate at a frequency of 120 Hz for a trans-glottal pressure of 1.2 kPa. Similar models created by Mantha *et al.* (in prep.) have exhibited onset pressures as low as 0.7 kPa for similar oscillation frequencies. Human phonation is normally initiated at a trans-glottal pressure of approximately 0.5 kPa.

Park *et al.* (in review) used synthetic driven models similar to those of Zhang *et al.* (2002), which were based on the M5 geometry and subjected to forced oscillations at a frequency of 100 Hz. The role of displacement flow on vortex formation was investigated. A more accurate procedure was developed for verifying the accuracy of the quasi-steady approximation. The influence of a comissure on the sound generation was also investigated (Park *et al.*, in review).

2.2 Mathematical Models and Theoretical Analysis of Phonation

Many mathematical models have been created to describe human phonation. Though all models are idealized representations, well constructed models may be used to provide additional insight into the physical phenomena involved in human phonation. Hypotheses generated by the observation of model behavior require experimental verification.

2.2.1. Model Classification

Structural models of the human vocal folds may be classified in terms of dimensionality. Models may be two-dimensional, three-dimensional, or hybrid. Phonation models may also be further categorized as reduced order or high order models. Reduced order models often consist of lumped spring-mass-damper systems designed to simulate the primary characteristics of the vocal folds with a minimum number of model parameters. Reduced order model simulations are computationally inexpensive, thus making them potentially useful to voice therapists and physicians. Higher order models may include thousands or millions of degrees of freedom (e.g. finite element and continuum models), but are computationally expensive. Higher order models may be used to examine the fundamental mechanisms of phonation which may not be modeled by reduced order models. Insight gained through the use of higher order models may be used to improve the accuracy of reduced order models.

2.2.2. Reduced Order Models

The first self-oscillating model of human phonation was created by Flanagan and Landgraf (1968). This model consisted of a single spring-mass-damper system subjected to an aerodynamic excitation described by Bernoulli's equation, and included acoustic loading. Lucero (2004) showed through mathematical analysis that a linear single mass model subjected to ideal fluid flow is not capable of self-oscillation. However, the addition of acoustic loading to such models has been shown to result in self-oscillation (Titze, 1988; Trevisan *et al.,* 2001).

The two-mass model of Ishizaka and Flanagan (1972) is one of the most cited studies in the field. In this study, fluid-induced oscillations of a lumped-element system consisting of two coupled masses, two viscous dampers, and three springs were investigated. Fluid flow was modeled using Bernoulli's Equation. Since the two-mass model was introduced, it has been widely utilized. Subsequent studies have analyzed more complex models having additional masses in both the inferior/superior direction as well as in the anterior/posterior direction (Kob, 2002). Recent reduced order models include a single rigid mass supported by two springs or an elastic base (Horçek and Sveç, 2002a), and a two-mass model in which both masses move in the medial/lateral direction, one of which has a rotational degree of freedom (Titze, 2002). Other studies include more sophisticated fluid models such Titze (1988) and Lamar *et al.* (2002). Analysis of these models has ranged from simple observations of the model's behavior to stability and bifurcation analysis (Horacek and Svec, 2002b; Lucero 1999).

2.2.3. Higher Order Models

Hunter *et al.* (2004) investigated the posturing which occurs prior to phonation using a finite element model of the cartilages and muscles involved in phonation. A finite element model was utilized by de Vries *et al.* (1999) to obtain more accurate values for the parameters of a reduced order model of the vocal folds. The stresses involved in the motion and collision of the vocal folds were examined by Gunter (2003) using a fully three-dimensional finite element model. The accuracy of these models is limited by a lack of tissue properties information. Parametric studies have been utilized to circumvent this limitation (Berry and Titze, 1996).

High order models have also been used to study the vibratory characteristics of the vocal folds. Modal analysis is the most common procedure used. Modal analysis provides the mode shapes and associated resonance frequency for each normal mode of vibration. Normal modes are the simplest building blocks of the complex vibration response of a linear system. The response of a linear system to an arbitrary forcing function may be viewed as consisting of a superposition of the systems' normal modes. Modal analysis of a solid "in vacuo" does not directly address the fluid-structure interactions which occur during phonation. However, knowledge of the vocal folds' modal properties can be used to better understand the behavior of the vocal folds when subjected to aerodynamic forces (Berry, 2001).

Berry and Titze (1996) reintroduced and expanded upon a continuum model of the vocal folds first proposed by Titze and Strong (1975). The vocal folds were idealized as a uniform rectangular parallelepiped fixed on three faces. The remaining three faces were free to vibrate, as shown in Figure 2.1. The updated study utilized more accurate boundary conditions and reported new observations on the modal characteristics of the continuum structure. Modal analysis was performed assuming a transversely orthotropic material. For a nearly incompressible material formulation, it was found that the second and third modes of vibration occurred at nearly the same frequency across a wide range of tissue properties. Superposition of these two modes was reported to result in a converging/diverging orifice geometry. It was conjectured that these two modes might both respond when the model was subjected to aerodynamic loading. The authors interpreted this result as supporting the converging/diverging orifice configuration theory of Titze (1988).

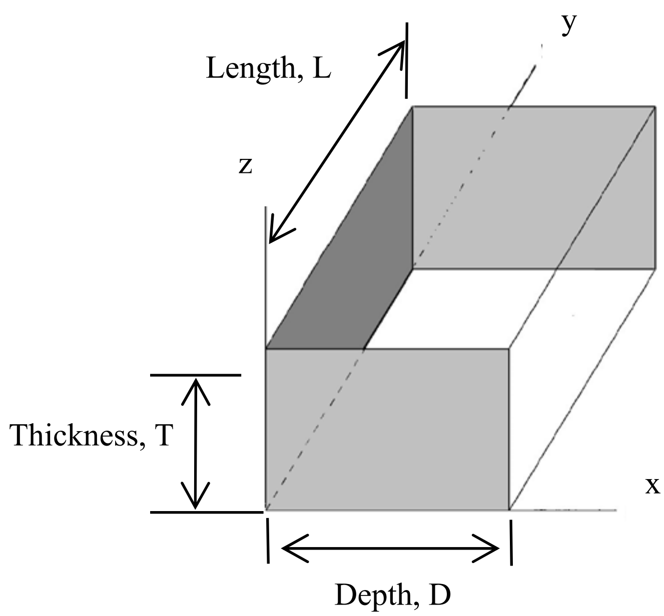

Figure 2.1: Schematic diagram of the continuum model (adapted from Berry and Titze, 1996). Shaded faces indicate fixed boundary conditions.

2.3 Motivation of the Present Study

Thomson (2004) verified the accuracy of a finite element fluid model for steady flow through an M5 glottis profile. However, a dynamic verification was not performed. The first objective of the present study was to determine the accuracy with which the same finite element numerical model is capable of predicting dynamic fluid flow representative of human phonation. A proper verification will support the use of this technique for future simulations of fluid flow through the human glottis.

de Vries *et al.* 2002 compared the different behavior of the two-mass model when subjected to viscous or ideal fluid flow. This study found that viscous, incompressible flow as modeled by the Navier-Stokes equations produced more realistic results than are obtained by the use of Bernoulli's equation. In the present work, a similar approach was used in which a viscous, incompressible fluid governed by the Navier-Stokes equations was coupled with a single spring-mass-damper system. Recall that a single-mass model may be induced to oscillate by the presence of acoustic loading (Flanagan and Landgraff, 1968), but that a single-mass model will not self oscillate when subjected only to ideal fluid flow (Lucero, 2004). The purpose of this work was to determine the effects of a more accurate fluid model on the stability of a simple model of the vocal folds. Such an investigation will provide more information concerning the role of viscous forces and flow structures on self-oscillation.

The literature on vocal fold modeling suggests that structural complexity is a key factor influencing self-oscillation. For example, the simple two-mass model will self oscillate when subjected to ideal flow (Ishizaka and Flanagan, 1972) whereas the one-mass model will not (Lucero, 2004). A clear understanding of the structural characteristics of the vocal folds will allow for the creation of more accurate phonation models. Furthermore, the validity and range of applicability of existing reduced order models depends upon the degree to which these models are able to accurately simulate the attributes of the human vocal folds. The continuum model of Berry and Titze (1996) was used to determine the model's sensitivity to its key dimensions (length, depth, and thickness) and to obtain descriptive information concerning the complex vibratory behavior of the continuum vocal fold model.

3. METHODS

In this chapter, the methods utilized in the present work are described. These include methods used for simulating the dynamic flow of air through a time varying orifice representative of the human glottis, numerical methods used to compute the fluid-structure interactions of a single degree-of-freedom model of the vocal folds, and methods used for obtaining vibratory normal modes of a continuum vocal fold model.

3.1 Numerical Methods Overview

The commercially available finite element package ADINA (an acronym for Automatic Dynamic Incremental Nonlinear Analysis) was used for all fluid flow simulations and fluid-structure interaction simulations in this study. This software was specifically designed to perform finite element analyses of structures, fluids, and fluid-structure interactions. Structural members may be modeled as linear or nonlinear, including material nonlinearities, large deformations and contact conditions. Static analysis, modal analysis, or transient analysis using explicit or implicit time integration can be performed.

Fluids can be modeled as laminar or turbulent, acoustic, incompressible or compressible fluids governed by the appropriate versions of the Navier-Stokes equations. All fluid simulations in the present study were performed assuming viscous incompressible fluid flow. The conservation of mass relation and Navier-Stokes equations for viscous incompressible flow are:

$$\nabla \cdot \mathbf{u} = 0 \tag{3.1}$$

$$\rho \frac{D\mathbf{u}}{Dt} = -\nabla P + \mu \nabla^2 \mathbf{u} \,. \tag{3.2}$$

In these equations, u is the vector of fluid velocities, ρ is the fluid density, P is the fluid pressure and μ is the fluid viscosity.

The fluid and structure may be either directly or iteratively coupled. In direct coupling, the fluid and structure matrices are combined and the resulting system solved as a whole at each time step. In the iterative method, the fluid and structure are solved separately. During each time step, the fluid and structure are iteratively solved until the fluid-structure interaction boundary conditions (summation of forces and continuity relations) are satisfied. The solver then marches on to the next time step. For simple systems, the direct method is faster. However, as the fluid and structure matrices become large, the combination of these two domains into a single matrix equation results in an oversized matrix. Because the solution time increases drastically with matrix size, the iterative method is generally faster for large, complex fluid-structure systems. Detailed information concerning the numerical formulations of ADINA as well as general finite element formulations may be found in Bathe (1996) and Cook *et al.* (2001).

3.2 Verification of Numerical Accuracy for Dynamic Fluid Flow Simulations

A numerical model was designed to determine the accuracy of the finite element fluid model introduced in Section 3.1. The experimental configuration of Park *et al.* (in review) was used to provide experimental data for direct comparison. Park *et al.* utilized a synthetic silicone model of the human vocal folds which was subjected to forced oscillations. The fluid flow through the synthetic model was measured using hot wire anemometry, pressure sensors, and flow meters. The fluid flow was assumed to be representative of human phonation. The numerical model was designed to match the experimental configuration of Park et al. (in review) as closely as possible. The modeling approximations which were applied to the numerical model are discussed in the following sections.

3.2.1. Two-Dimensional Analysis Assumption

The physical model of Park *et al.* was a three-dimensional structure representative of the human vocal folds. The model possessed two symmetry planes, one passing through the center of both moving "folds" (a coronal plane) and another passing along the line formed by the folds when completely closed (the mid-sagittal plane). The coronal plane was chosen for two-dimensional fluid flow analysis. This approximation significantly reduces computational expense. It also introduces discrapancy between the experiment and the numerical calculations by precluding the simulation of asymmetric flow behavior. A photo of the synthetic vocal fold model is shown in Figure 3.1.

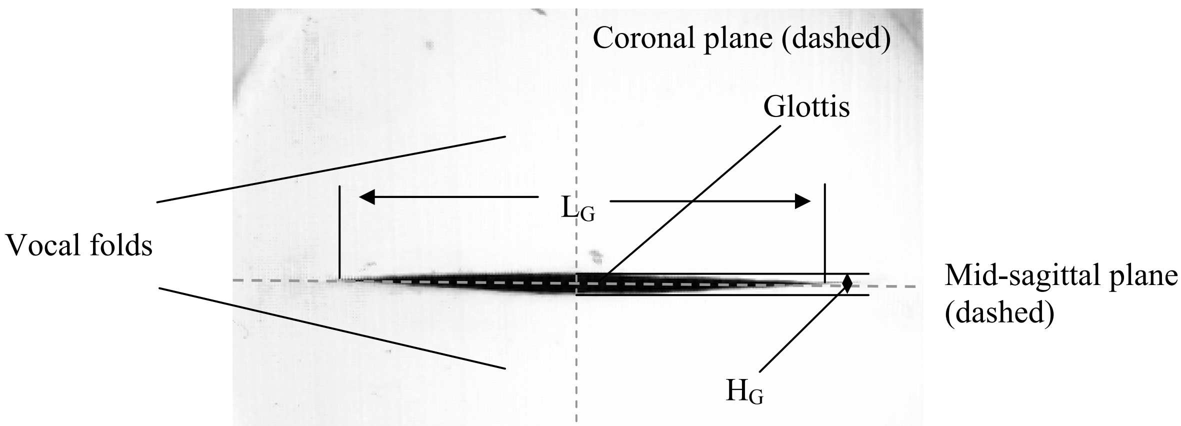

Figure 3.1: The synthetic vocal fold model as viewed from a point downstream from the orifice.

A two-dimensional representation effectively models the vocal folds as infinitely long structures. The orifice aspect ratio, *AR*, may be defined as the ratio of the orifice length, L_O , to the orifice height, H_O:

$$AR = \frac{L_O}{H_O}. \tag{3.3}$$

An infinitely long structure would have an infinite aspect ratio. The orifice aspect ratio ranges from a minimum value of approximately 17 at maximum opening to a very large value just before closure. Examination of the flow field velocity (Park *et al.,* in review) indicated that the fluid velocity at the orifice center is nearly constant in the lengthwise direction. The previous two observations provide adequate justification for making the two-dimensional simplification. It should be noted that the flow field solution obtained in this manner is restricted to the symmetry plane only. Since the purpose of this analysis was only to verify the accuracy of the flow model, this limitation was deemed acceptable.

Symmetry of the flow field was assumed in order to reduce the size of the fluid domain, thereby reducing computational effort. Only the lower half of the coronal symmetry plane was modeled and analyzed. A simplified diagram of the coronal symmetry plane is shown in Figure 3.2.

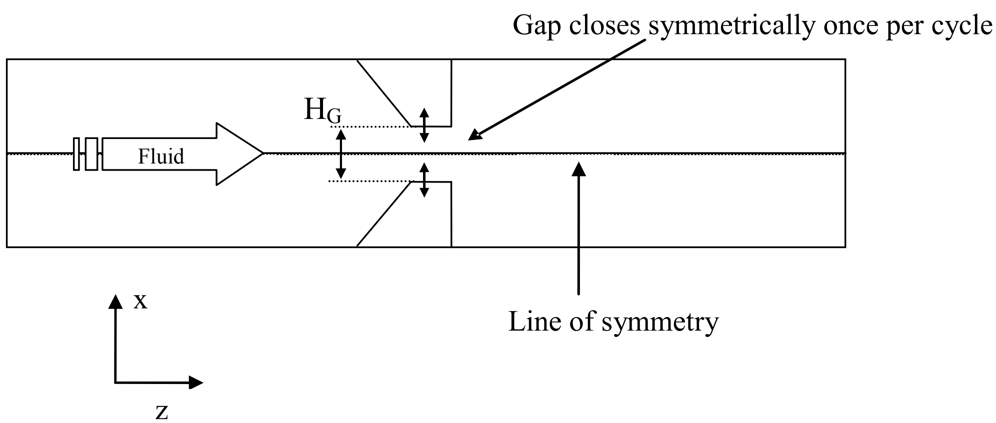

Figure 3.2: Schematic representation of the coronal symmetry plane.

3.2.2. The Assumption of Negligible Structural Deformation

In the experimental setup of Park *et al.* (in review) the motion of the vocal fold model was imposed by actuators operating at a constant frequency of 100 Hz. Because the actuator forces were estimated to be several orders of magnitude greater than aerodynamic forces, the influence of aerodynamic forces on structural displacements were neglected. This assumption reduces the complexity of the system from a fully coupled fluid-structure interaction problem to that of a fluid constrained to move through an orifice of varying size. The motion of the wall was enforced upon the computational fluid domain without considering the fluid's effect upon wall motion.

Upon inspection of the silicone compound used to create the physical model, it was assumed that small deformations of the vocal fold walls would have very little effect on fluid flow compared to the large-amplitude motion of the model's orifice. Also, because the purpose of these simulations was to obtain detailed flow field information, the stresses in the physical model were of little consequence. Thus, the structural response was not considered. The fluid analysis was performed using the finite element program described in Section 3.1. The orifice motion was prescribed by applying a "moving wall" boundary condition.

3.2.3. Fluid Assumptions

The flow was considered to be incompressible. The fluid properties reflected the conditions matched those measured in the laboratory on the day of the experiment. Temperature and pressure were measured directly using a thermometer and barometer, respectively. Viscosity was obtained from tabulated data for air viscosity as a function of temperature (Fox and MacDonald, 2003). Density was calculated according to the Ideal Gas Law:

$$PV = mRT \tag{3.4}$$

where P is pressure (Pa), V is volume (m^3), m is mass (kg), R is the gas constant for air, and T is the temperature (K). Density may be expressed in terms of the two measured quantities, temperature and pressure:

$$\rho = \frac{P}{RT}. \tag{3.5}$$

Under adiabatic assumptions the bulk modulus may be calculated as follows:

$$K = \gamma P\,. \tag{3.6}$$

where γ is the ratio of the constant-pressure specific heat to the constant-volume specific heat. Table 3.1 lists the fluid properties which were used.

Table 3.1: Fluid properties used in numerical simulations.

Property	Value
Temperature	78° F / 25. 6° C
Pressure	748 mmHg / 99.7 kPa
Viscosity	1.864E-5 kg/(m·s)
Density	1.16 kg/m^3
Bulk Modulus	139.6 kPa
Ratio of specific heats, γ	1.4

3.2.4. Geometry and Boundary Conditions

An 8 cm x 1.75 cm channel was considered with a trapezoidal protrusion located 2.5 cm downstream from the inlet. The protrusion geometry was based on the dimensions of the synthetic model. Figure 3.3 shows the geometry, boundary conditions, and computational grid of the fluid domain.

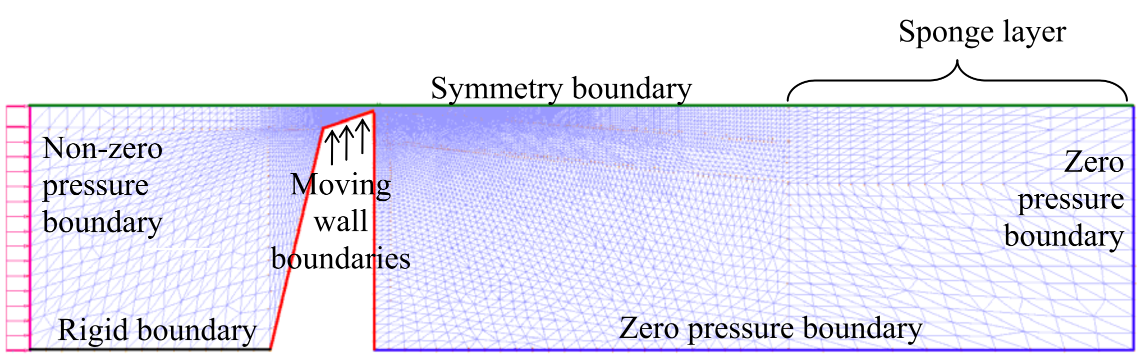

Figure 3.3: Geometry, boundary conditions, and computational mesh of the numerical model.

To match the experimental configuration, a uniform zero pressure boundary was imposed 5 cm downstream from the orifice along the right vertical boundary as well as along the lower boundary downstream of the orifice.

Acoustic measurements were not recorded during the experiment. Static pressure measurements at a location 2.5 cm upstream from the orifice indicated that a 1.05 kPa pressure drop occurred between this point and the atmospheric conditions downstream from the orifice. In the numerical model, a uniform 1.05 kPa constant pressure surface was applied 2.5 cm upstream from the orifice at the left vertical boundary. The absence of fluctuating pressure boundary conditions may have introduced discrepancies between the simulation and experiment.

A layer of more viscous fluid was used to reduce the effect of non-physical pressure reflections which may occur when a vortex encounters a zero pressure boundary. This so-called "sponge layer" consisted of a fluid identical to that described above except that the viscosity of the sponge layer fluid was ten times greater than that of air. This layer served to dissipate any vortices before they encountered the zero pressure boundary.

The top edge (which is the line of symmetry and the center line of the channel), was defined as a symmetric boundary condition: the flow along this line was tangential to the boundary. The lower boundary upstream of the orifice was defined as a solid wall with friction ("no slip" boundary condition).

3.2.5. Structural Motion

High speed images taken during the experiment were used to determine the motion of the model at the coronal plane. The orifice height was obtained by measuring the number of pixels separating the two halves of the model at each time increment. The known length of the orifice (17 mm) provided a reference for conversion between pixels and millimeters. The resulting data was used to specify the motion of the protrusion in the numerical simulation. This orifice height time history is shown in Figure 3.4.

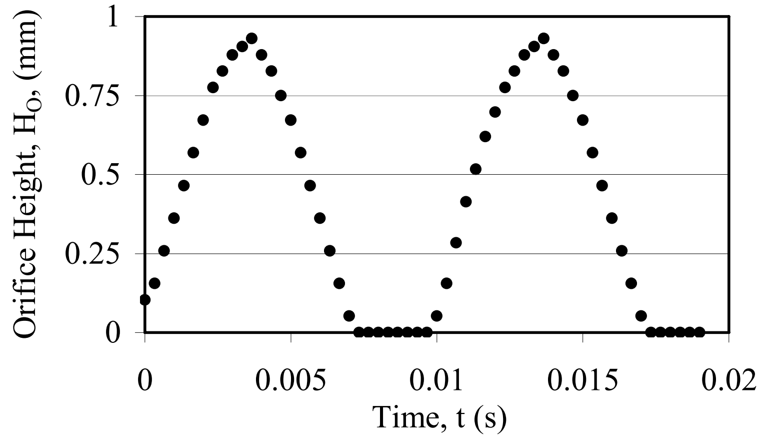

Figure 3.4: Orifice height time history.

3.2.6. Gap Condition

A "gap condition" was used to interrupt the fluid flow through the orifice while preventing collision between the upper wall and the protrusion. Because triangular fluid elements were used, a collision of this type would have resulted in elements of zero volume, thus leading to a numerical singularity. The gap condition prevents fluid from passing through the orifice when the gap between the upper and lower walls reaches a specified value. A gap size, G = 0.011 mm was adopted during closure. A slightly greater gap, G = 0.012 mm was used during opening. The discrepancy between opening and closing gap size values was to avoid numerical instability (*ADINA Theory and Modeling Guide Volume III,* 2004). Note that the gap size G, is a parameter of the numerical model. Because the numerical model utilizes symmetry, the orifice height, H_O, is related to the gap size by the following relation:

$$G = \frac{H_O}{2}. \tag{3.7}$$

3.2.7. The Finite Element Mesh

The fluid domain was meshed with three-node triangular elements designed for incompressible flows. The grid consisted of 28 000 elements. A sketch of the grid is shown in Figure 3.3. High mesh density was utilized in regions of high pressure or velocity gradients. A somewhat coarser grid was used in areas of low gradients. Care was taken to ensure a smooth transition between areas of high and low mesh density. Mesh refinement was performed in order to determine that the mesh represented a converged solution.

The orifice region experiences extreme mesh distortion as the orifice gap varies from G = 0.01 mm to G = 0.465 mm. In order to minimize element distortion due to extension and contraction, the model was constructed such that during each complete oscillation, each element was extended and compressed by the same factor. This may be expressed using the following equations:

$$\frac{G_0}{MF} = G_{\min} \ , \tag{3.8}$$

$$G_0 \cdot MF = G_{\max} \ , \tag{3.9}$$

where G_0 is the initial distance between the upper and orifice walls, $G_{\min}$ is the minimum gap distance (0.01 mm), $G_{\max}$ is the maximum gap distance (0.465 mm), and MF is the magnification factor. The two unknowns, MF and G_0 were found to be 6.82 and 0.068 mm, respectively. The use of these values minimized distortion of the computational grid.

Simulation results for fluid flow simulations through a synthetic model of the human glottis are presented and discussed in Chapter 4.

3.3 Single Degree-of-Freedom Models of the Vocal Folds

As was noted by Lucero (2004), a single-mass model coupled with Bernoulli flow is not capable of simulating sustained oscillation. In order to investigate the effects of viscous flow on an idealized lumped mass model, a rigid mass-spring-damper system was coupled to a viscous fluid domain similar to that of Section 3.2. The mass, spring and damper values were selected to produce vibration on the order of that observed in human phonation. A schematic representation of this model is shown in Figure 3.5.

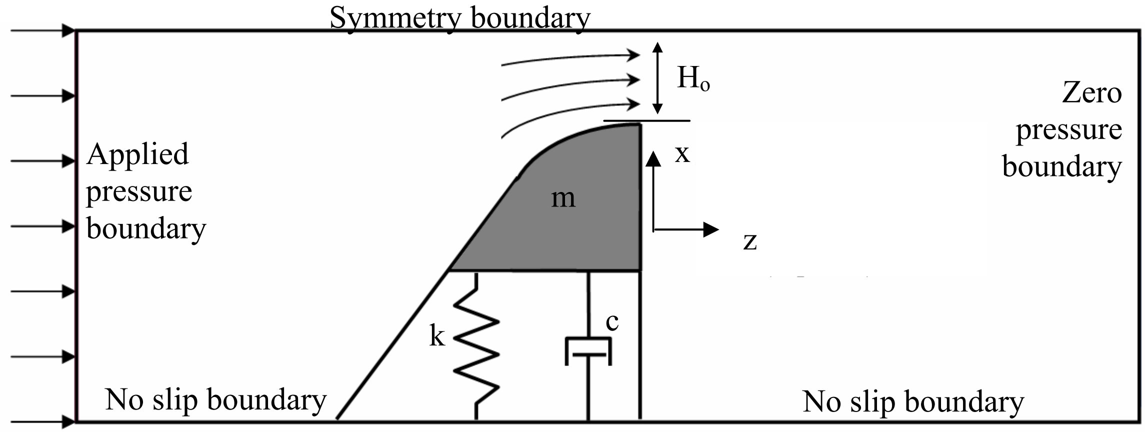

Figure 3.5: Schematic representation of the one mass model; m = 0.046 kg; k = 5000 N/m; c = 4 kg/s; initial H_O = 2 mm.

3.3.1. Modeling Assumptions Applied to the Single Mass Model

The fluid was modeled as incompressible and viscous. Flow symmetry was assumed. Static boundary conditions were applied to the computational domain. The structure was modeled as a rigid lumped mass. Discrete spring and damper elements were used as shown in Figure 3.5. The mass was constrained to move in the x-direction. No collisions between the mass and the upper wall were permitted.

3.3.2. Structural Model Assumptions

The M5 geometry (Scherer *et al.,* 2001), was used to define the glottal profile on a scale representative of human phonation. A very high Young's Modulus (E = 10^{13} Pa) was assigned to the mass in order to model this region as rigid. All finite element nodes within the mass were constrained to move in the x-direction. No rotation of the mass was allowed.

Linear spring and damping elements were used to provide stiffness and damping characteristics. Although the mass itself was assigned a density of zero, the spring element was assigned a discrete mass value which was constant and independent of the area of the mass region.

3.3.3. Computational Considerations

In order to avoid the numerical singularities associated with fluid elements of zero volume, collisions between the mass and the upper wall of the fluid domain were not allowed. This does not preclude self-oscillation. The falsetto voice register has been observed in which no collisions are present (Svec, 2002). Thomson (2005) created a self-oscillating numerical model of phonation in which collisions were absent.

The structural region was meshed with approximately 300 plane strain quadratic elements. The fluid region was meshed with approximately 18 000 planar fluid elements. Exact numbers of elements varied slightly depending on the structural geometry. The fluid and solid meshes are shown in Figure 3.6. Because the structure in this case is very simple (only several hundred elements), the direct solution technique was used for all fluid-structure interaction simulations. Single-mass model simulation results are presented and discussed in Chapter 5.

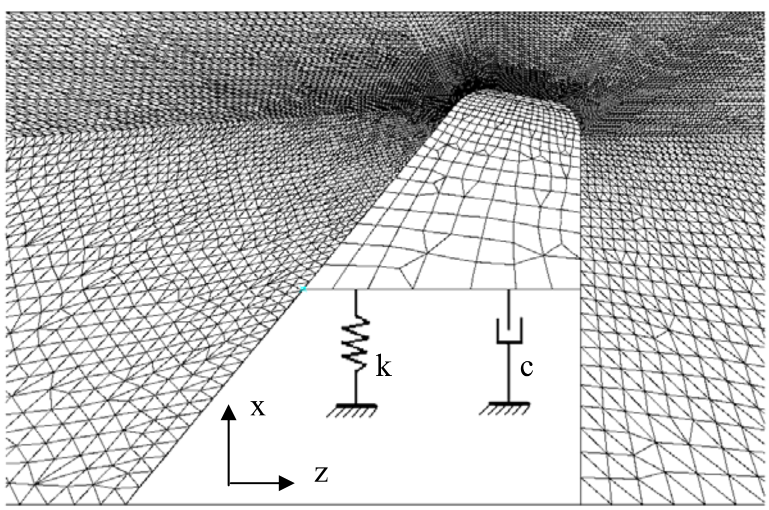

Figure 3.6: Computational grid for solid and fluid domains with schematic representation of spring and damper elements.

3.4 Modal Analysis of an Idealized Model of the Vocal Folds

An idealized continuum model of vocal fold tissue was used to investigate the modal properties of the vocal folds. Computational techniques included both the Ritz and finite element methods (ADINA).

3.4.1. The Continuum Model

The continuum model of Berry and Titze (1996) was used to investigate the dimensionality of the vocal folds structure. The continuum model consists of a solid rectangular parallelepiped of uniform material properties. The model is subjected to the following boundary conditions: 1) no motion allowed on anterior/posterior and lateral faces 2) free motion allowed on the inferior/superior and medial faces. The model and accompanying boundary conditions are shown in Figure 2.1.

The continuum model shown in Figure 2.1 consisted of a uniform, linearly elastic, transversely isotropic rectangular solid. A transversely isotropic material possesses the same material properties in all directions within the transverse plane, and different properties in the longitudinal direction, which is perpendicular to the transverse plane. The xz plane of Figure 2.1 is the transverse plane and the longitudinal direction is parallel to the y-axis. This type of material was selected in order to approximate the vocal fold tissue, which consists of muscle fibers along the anterior/posterior direction.

The stress-strain relationships of a three-dimensional transversely isotropic material may be described using Hooke's Law,

$$[\sigma] = [C][\varepsilon] \ , \tag{3.10}$$

where $[\sigma]$ is the vector of six stress components,

$$[\sigma] = \begin{pmatrix} \sigma_{xx} \\ \sigma_{yy} \\ \sigma_{zz} \\ \tau_{xy} \\ \tau_{yz} \\ \tau_{zx} \end{pmatrix}, \tag{3.11}$$

[ε] is the vector of six strain components,

$$[\varepsilon] = \begin{pmatrix} \varepsilon_{xx} \\ \varepsilon_{yy} \\ \varepsilon_{zz} \\ \gamma_{xy} \\ \gamma_{yz} \\ \gamma_{zx} \end{pmatrix} \tag{3.12}$$

and [C] is the matrix of elastic coefficients. The inverse matrix, $[C]^{-1}$ has a simpler form and is expressed as,

$$[C]^{-1} = \begin{bmatrix} \frac{1}{E_{trans}} & -\frac{\nu'}{E'} & \frac{\nu_{trans}}{E_{trans}} & 0 & 0 & 0 \\ -\frac{\nu'}{E'} & \frac{1}{E'} & -\frac{\nu'}{E'} & 0 & 0 & 0 \\ \frac{\nu_{trans}}{E_{trans}} & -\frac{\nu'}{E'} & \frac{1}{E_{trans}} & 0 & 0 & 0 \\ 0 & 0 & 0 & \frac{1}{\mu'} & 0 & 0 \\ 0 & 0 & 0 & 0 & \frac{1}{\mu'} & 0 \\ 0 & 0 & 0 & 0 & 0 & \frac{1}{\mu_{trans}} \end{bmatrix}. \tag{3.13}$$

A uniform transversely isotropic material possesses five independent material constants. These are the Young's modulus and Poisson's ratio in the transverse plane (E_{trans} and ν_{trans}), the Young's modulus, Poisson's ratio and shear modulus in the longitudinal direction (E', v', and μ'). The shear modulus in the transverse plane (μ_{trans}) depends upon Young's modulus and Poisson's ratio in the transverse plane through the relation

$$\mu_{trans} = \frac{E_{trans}}{2(1+\nu_{trans})} . \tag{3.14}$$

In terms of standard material constants, the transverse and longitudinal material constants are,

$$E_{trans} = E_x = E_z, \tag{3.15}$$

$$E_{long} = E_y, \tag{3.16}$$

$$v_{trans} = v_{yz} = v_{xy}, \tag{3.17}$$

$$v_{long} = v_{xz} , \tag{3.18}$$

$$\mu_{long} = \mu_{xy} = \mu_{yz} . \tag{3.19}$$

The material properties used in this study were the same as those used by Berry and Titze (1996), and are listed in Table 3.2.

Table 3.2: Model dimensions and tissue properties.

	CGM Units	SI Units
Lateral depth, D	1.0 cm	0.01 m
Longitudinal (anterior-posterior) length, L	1.2 cm	0.012 m
Vertical thickness, T	0.7 cm	0.007 m
Tissue density, ρ	1.03 g/cm^3	1030 kg/m^3
Transverse Young's modulus, E_{trans}	10^5 dyne/cm2	10^4 Pa
Longitudinal shear modulus, μ_{trans}	10^5 dyne/cm2	10^4 Pa
Transverse Poisson's ratio, v_{trans}	0.9999	0.9999
Longitudinal Poisson's ratio, v'	0	0

Modal analysis of this structure was performed using two methods: the Ritz Method and the finite element method. Additional assumptions were made as discussed below.

3.4.2. Modal Analysis

Modal analysis is a common procedure whereby resonance frequencies of a structure are obtained by the solution of an eigenvalue problem of the form:

$$\mathbf{A}\,\mathbf{x} = \lambda\,\mathbf{B}\,\mathbf{x} \tag{3.20}$$

Where **A** is the structure's stiffness matrix, **B** is the structure's mass matrix, **x** is the eigenvector and λ being the corresponding eigenvalue. There are a variety of methods which have been developed for obtaining the matrices **A** and **B**. Some of these include the Rayleigh-Ritz Method, weighted residuals methods, and the Galerkin Method (Meirovitch, 1997). Numerous methods also exist for solving the eigenvalue problem once the mass and stiffness matrices have been obtained.

Two assumptions are common to standard modal analysis formulations: 1) linear elasticity and 2) the structure exists *in vacuo*. Linear superposition allows complex vibration responses to be decomposed into a linear superposition of linear normal modes. However, linearity also requires that the displacement fields remain within the limits of the small amplitude assumption. Thus, many types of vibration which are inherently nonlinear cannot be analyzed using modal analysis.

Unless fluid contributions are explicitly included in the analysis of a structure, modal analysis neglects fluid forces. This simplification is reasonable for structures which are relatively insensitive to the influences of a surrounding fluid. Thus, aerodynamic forces which are present in and vitally important to actual phonation are neglected by modal analysis. However, Berry (2001) has observed that the linear, *in vacuo* normal modes of vibration are qualitatively similar to those obtained empirically from in vivo experiments using canine larynges.

3.4.3. Modal Analysis of the Continuum Model via the Ritz Method

The Ritz method is based upon the principle of minimum potential energy. Displacement functions were used to approximate the mode shapes of the structure of interest. Displacement functions must satisfy essential boundary conditions, such as zero displacement, while being flexible enough to describe a wide variety of vibratory shapes. Polynomials were used as the shape functions in the x- and z-directions while sinusoidal functions were used to approximate displacements in the y-direction as in (Berry & Titze, 1996). Thus,

$$\xi(x, y, z, t) = \sin(\omega t)\sin\left(\frac{\pi y}{L}\right)\sum_{i=1}^{I}\sum_{j=0}^{J} A_{ij} x^i z^j \tag{3.21}$$

$$\psi(x, y, z, t) = 0 \tag{3.22}$$

$$\varsigma(x, y, z, t) = \sin(\omega t)\sin\left(\frac{\pi y}{L}\right)\sum_{m=1}^{M}\sum_{n=0}^{N} B_{mn} x^m z^n \tag{3.23}$$

where $\xi(x,y,z,t)$, $\psi(x,y,z,t)$, and $\zeta(x,y,z,t)$ represent displacement functions in the x-, y-, and z-directions, respectively. One important assumption which significantly simplified the analysis was that all displacements in the y-direction were neglected (Eqn. 7b). This assumption was originally based upon observations of excised canine larynges which led to the conclusion that vocal fold motion was restricted to the coronal plane (Saito *et al.,* 1985). A more recent study by Berry *et al.* (2001), confirmed that the vibration of vocal fold along the medial surface was composed primarily of motion in the x-(medial/lateral) and z-(inferior/superior) directions. Vibration amplitude the y-(anterior/posterior) direction was observed to be approximately one order of magnitude lower than that found in the x-and z-directions. Thus, constraint of y-direction displacement is consistent with recent quantitative measurements and significantly reduced computational time. The consequences of the planar motion assumption are discussed in Section 4.3.

The potential energy of the continuum may be expressed as;

$$\Pi = I_1 - \omega^2 I_2 \tag{3.24}$$

where,

$$I_1 = \frac{1}{2}\int_{z=0}^{T}\int_{y=0}^{L}\int_{x=0}^{D} \varepsilon^T C\,\varepsilon\;dx\,dy\,dz \tag{3.25}$$

$$I_2 = \frac{\rho}{2}\int_{z=0}^{T}\int_{y=0}^{L}\int_{x=0}^{D} (\xi^2 + \varsigma^2)\;dx\,dy\,dz \tag{3.26}$$

as given by Washizu (1968). Here, I_1 represents the internal strain energy and I_2 represents the kinetic energy of the structure. The potential energy is calculated using the integral expressions given above, then rendered stationary by differentiation with respect to each unknown coefficients A_{ij} and B_{mn};

$$\frac{\partial \Pi}{\partial A_{ij}} = 0 \quad \left(i = 1,2,3,...I;\, j = 0,1,2....J\right) \tag{3.27}$$

$$\frac{\partial \Pi}{\partial B_{mn}} = 0 \quad \left(m = 1,2,3,...M;\, n = 0,1,2....N\right) \tag{3.28}$$

This yields a set of equations which must be simultaneously solved in order to obtain the system eigenvalues.

Equations (3.21) and (3.22) yielded a set of a equations which were quadratic with respect to the unknown constants A_{ij} and B_{mn}. Differentiation by A_{ij} and B_{mn} as stated in Equations (3.23) and (3.24) resulted in a set of equations which were linear in the coefficient of differentiation. The coefficients were then ordered according to the following scheme,

$$\begin{aligned}\mathbf{x}^T &= [v_1, v_2, v_3, ...v_K] \\ &= [A_{10}, A_{11}, A_{12}, ...A_{ij}, B_{10}, B_{11}, B_{12}, ...B_{mn}]\end{aligned}. \tag{3.29}$$

Finally, the individual numerical terms of each equation were isolated by differentiation with respect to each unknown coefficient. The system of equations may then be expressed as stiffness (**K**) and mass (**M**) matrices:

$$\mathbf{K} = \begin{pmatrix} \frac{\partial^2 I_1}{\partial {v_1}^2} & \frac{\partial^2 I_1}{\partial v_1 \partial v_2} & \frac{\partial^2 I_1}{\partial v_1 \partial v_3} & \cdots \\ \frac{\partial^2 I_1}{\partial v_2 \partial v_1} & \frac{\partial^2 I_1}{\partial {v_2}^2} & \frac{\partial^2 I_1}{\partial v_2 \partial v_3} & \cdots \\ \frac{\partial^2 I_1}{\partial v_3 \partial v_1} & \frac{\partial^2 I_1}{\partial v_3 \partial v_2} & \frac{\partial^2 I_1}{\partial {v_3}^2} & \cdots \\ \vdots & \vdots & \vdots & \ddots \end{pmatrix} \tag{3.30}$$

$$\mathbf{M} = \begin{pmatrix} \frac{\partial^2 I_2}{\partial {v_1}^2} & \frac{\partial^2 I_2}{\partial v_1 \partial v_2} & \frac{\partial^2 I_2}{\partial v_1 \partial v_3} & \cdots \\ \frac{\partial^2 I_2}{\partial v_2 \partial v_1} & \frac{\partial^2 I_2}{\partial {v_2}^2} & \frac{\partial^2 I_2}{\partial v_2 \partial v_3} & \cdots \\ \frac{\partial^2 I_2}{\partial v_3 \partial v_1} & \frac{\partial^2 I_2}{\partial v_3 \partial v_2} & \frac{\partial^2 I_2}{\partial {v_3}^2} & \cdots \\ \vdots & \vdots & \vdots & \ddots \end{pmatrix}. \tag{3.31}$$

The matrix representation of the K stationary equations may then be expressed as;

$$\mathbf{Kx} = \omega^2 \mathbf{Mx}. \tag{3.32}$$

This system of equations was solved via standard eigenvalue techniques to obtain eigenvalues and eigenvectors.

The Ritz method was implemented using MATLAB. Integration and differentiation procedures for the creation of mass and stiffness matrices were carried out symbolically in order to reduce numerical errors. Only the eigenvalue problem was solved numerically. A more thorough description of this method may be found in Berry and Titze (1996).

3.4.4. Modal Analysis of the Continuum Model using the Finite Element Method

The finite element program ADINA (version 8.2) was also used to compute the normal modes of the continuum model. Like the Ritz Method, the finite element modal analysis also assumes linearity. This restricts the solution to small-amplitude oscillations about a state of equilibrium. Unlike the Ritz Method, the finite element method utilizes a large number of low-order polynomial-based elements in order to describe the mode shapes. Because of this, the finite element method can more accurately approximate complex mode shapes which are difficult to predict *a priori*.

The rectangular domain, shown in Figure 3.7, was meshed using 840 quadratic (27 node) three-dimensional solid finite elements for a total of 7875 nodal points. Repeated calculations using varying mesh densities confirmed that this configuration represents a mesh-converged solution. The model geometry and boundary conditions were consistent with Table 3.1. Modal analysis was performed in ADINA using the Lanczos solution method (*ADINA Theory and Modeling Guide I*, 2004).

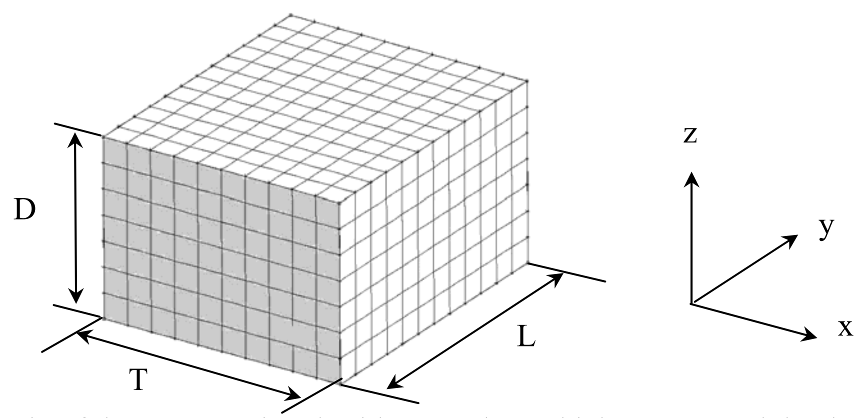

Figure 3.7: Schematic of the computational grid. Length, L, thickness, T, and depth, D shown. Shaded face indicates fixed boundary condition.

Aside from differences associated with approximating mode shapes, the Ritz and finite element method are generally considered to be alternate representations of the same problem. Both methods generate mass and stiffness matrices, then solve the linear system to obtain eigenvectors (mode shapes) and eigenvalues (modal frequencies). Thus, for the same assumptions, the Ritz and finite element methods should produce identical results. Modal analysis results are presented and discussed in Chapter 6.

4. FLOW SIMULATIONS RESULTS

Numerical predictions of the flow through a moving wall orifice are presented and compared to experimental data. The velocity profile across the orifice and velocity time history at the orifice center were both compared to measured values. The goal was to determine the accuracy of the finite element program introduced in Section 3.1 when used to simulate dynamic fluid flow representative of human phonation.

4.1 Numerical Convergence

Velocity values were obtained from both synthetic and numerical models one millimeter downstream from the orifice. Because of the symmetry which was assumed in the creation of the numerical model, a symmetric velocity profile was obtained across the orifice at each time step. Time history comparisons at a given point (the orifice center) and velocity profile comparisons across the orifice at a given instant in time were made.

Mesh convergence was evaluated by comparing the velocity profiles at the instant of maximum opening for several different mesh densities as shown in Figure 4.1. Subsequent results presented herein were obtained using the finest mesh.

Time step convergence was evaluated by decreasing the time step, Δt, while using the finest mesh obtained above. The velocity time history at the orifice center is compared for various time steps in Figure 4.2. A timestep of $\Delta t = 1x(10^{-4})$ seconds was used for all results hereafter.

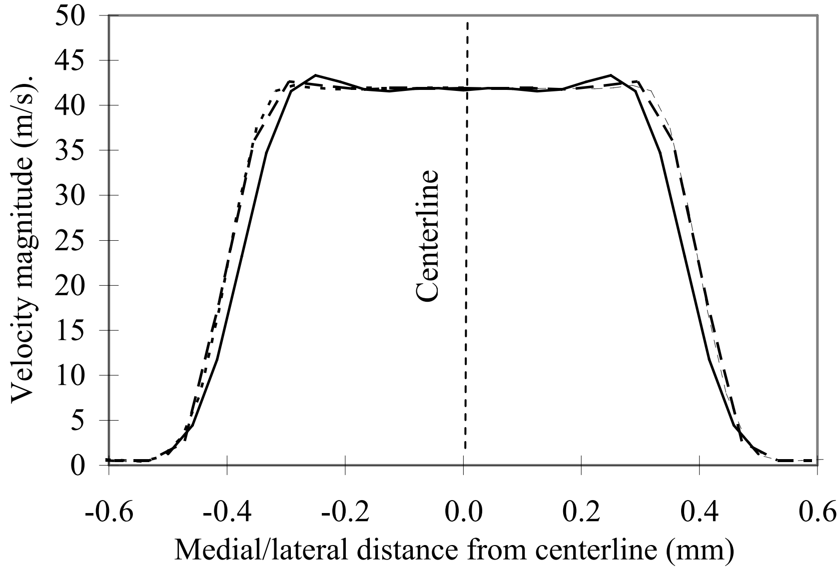

Figure 4.1: Axial velocity magnitude versus medial/lateral distance from orifice centerline at maximum orifice opening using numerical meshes of differing density; — Mesh 1 – 10 000 fluid elements; – – Mesh 2: 23 000 fluid elements; · · · Mesh 3: 28 000 fluid elements.

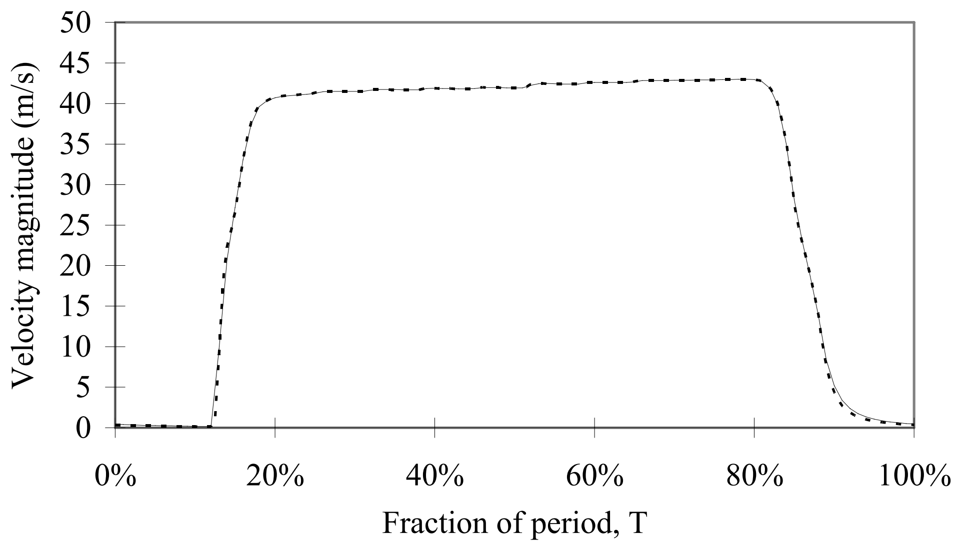

Figure 4.2: Axial velocity magnitude versus fraction of period, T.
— $\Delta t = 1x(10^{-4})$ s; – – $\Delta t = 0.5x(10^{-4})$ s

4.2 Flow Field Results

The velocity profile across the orifice was computed. Results from this simulation were compared to measured values at several discrete moments in time: *t* = T/4, *t* = T/2, and *t* = ¾ T, where *t* is the period of oscillation. These results are shown in Figures 4.3, 4.4 and 4.5.

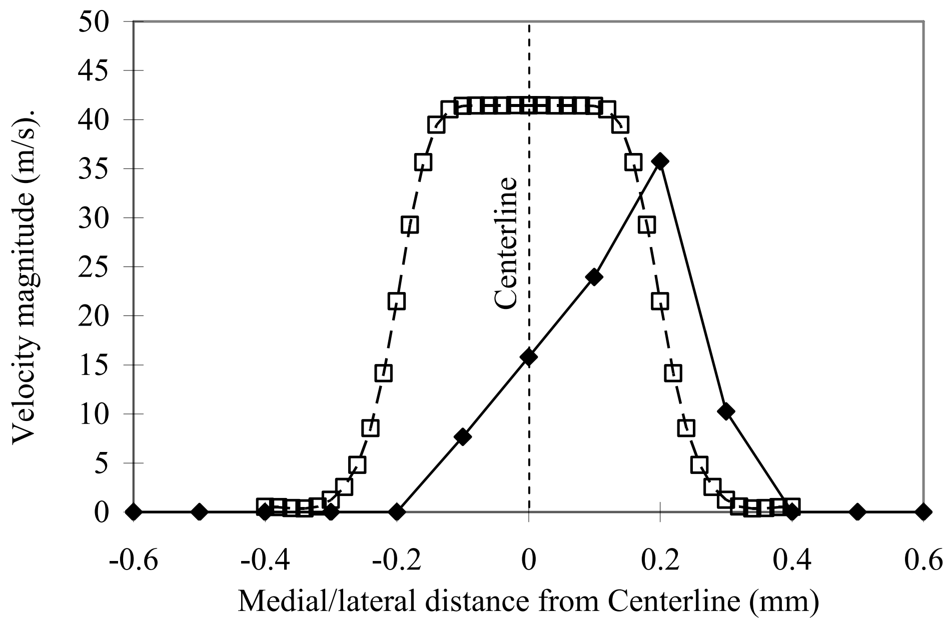

Figure 4.3: Axial velocity magnitude versus distance from centerline at *t* = T/4:
◆ - Experimental data; □ - Numerical predictions

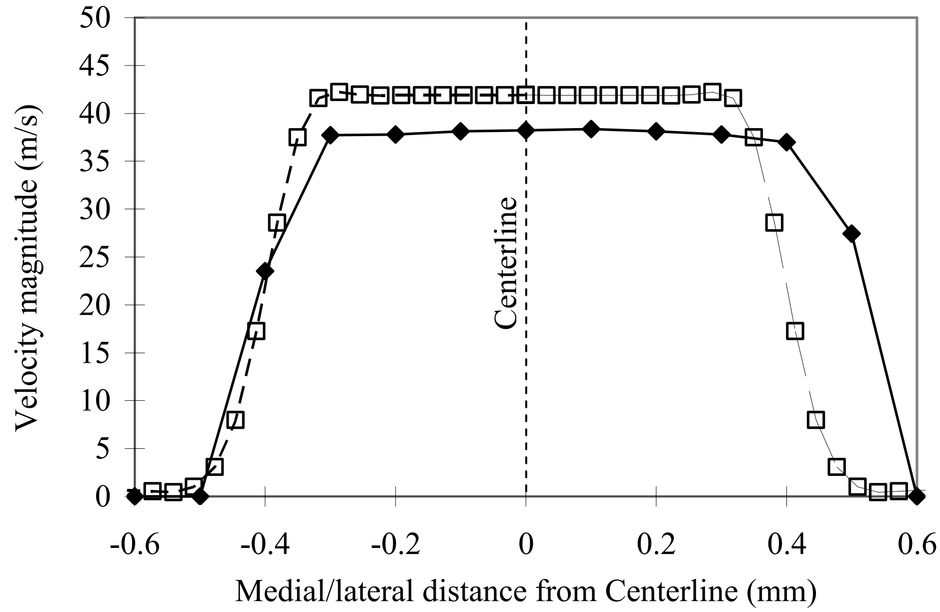

Figure 4.4: Axial velocity magnitude versus distance from centerline at *t* = T/2:
◆ - Experimental data; □ - Numerical predictions

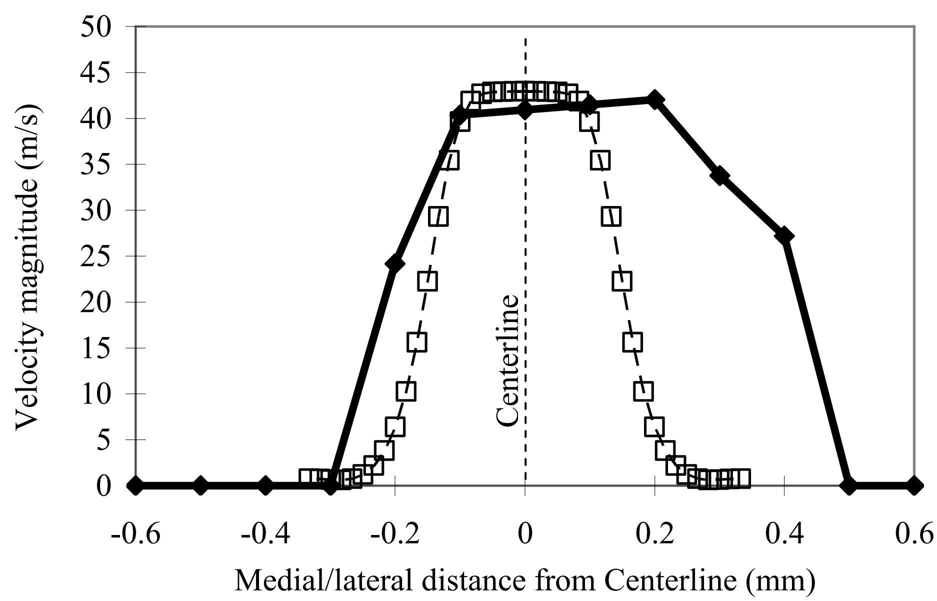

Figure 4.5: Axial velocity magnitude versus distance from centerline at *t* = 3T/4:
◆ - Experimental data; □ - Numerical predictions

A comparison between measured and predicted centerline flow velocity as a function of time is shown in Figure 4.6.

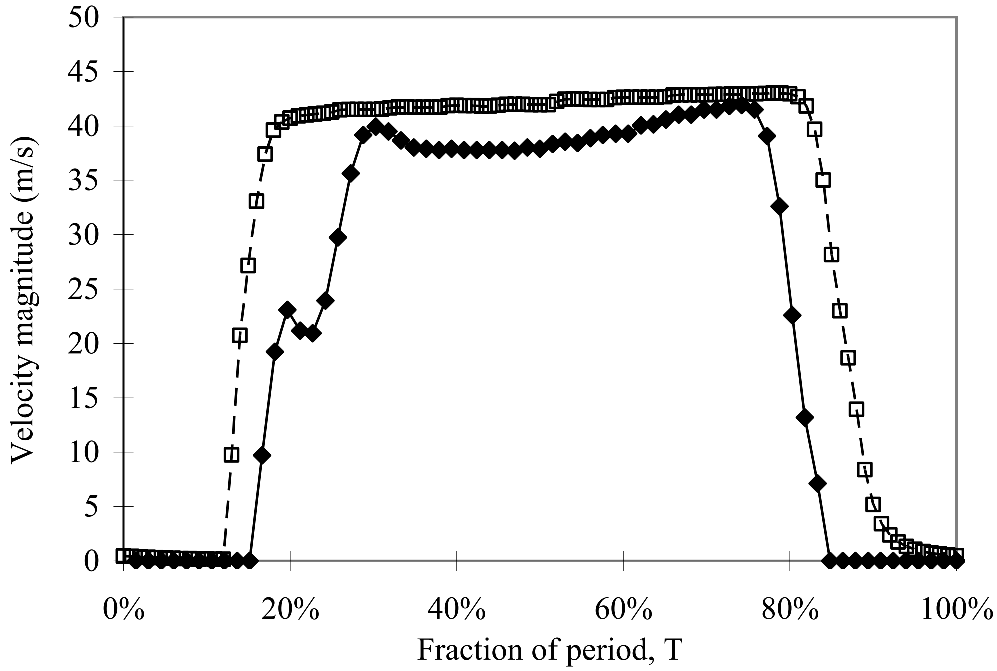

Figure 4.6: Flow velocity magnitude versus fraction of period, T, at orifice center:
◆ - Experimental data; □ - Numerical predictions

4.3 Discussion

4.3.1. Qualitative Accuracy of the Driven Model Simulations

The velocity time history at the orifice center is shown in Figure 4.6. It may be observed that both the rate of velocity increase and the rate of velocity decrease are correctly predicted by the numerical model. After reaching a peak velocity at approximately t = 0.3 T, the measured experimental velocity decreases slightly until

t = 0.4 T at which time it rises steadily to another peak value at t = ¾ T. The numerical model does not exhibit the first peak, but does rise steadily until reaching the second peak.

In the experimental case, the jet begins with a moderate width at t = T/4, increases in width at t = T/2, then decreases in width at t = ¾ T. Meanwhile, the maximum jet velocity increases during each of these periods. Similarly, the simulated jet is of moderate width at t = T/4, widens during the middle portion of the cycle, and finally narrows at t = ¾ T. As in the experimental case, the maximum velocity increases steadily.

4.3.2. Quantitative Accuracy of the Driven Model Simulations

The predicted and measured jet widths were not consistently in agreement as shown in Table 4.1. The jet width was defined as the width of the jet at the point where fluid velocity was equal to 5% of the core velocity. The percent difference values were calculated with reference to the experimental data. The calculated and measured jet widths are relatively similar at t = T/4 and t = T/2 case. The predicted jet width is much smaller than the measured jet width at t = ¾ T case.

Table 4.1: Jet width (mm).

	Predicted	Measured	Difference
t = T/4	0.57	0.49	16 %
t = T/2	0.98	1.08	9 %
t = ¾ T	0.47	0.79	- 41%

The maximum jet velocity, however, was predicted reasonably well by the numerical model. The error in maximum jet velocity was 16%, 20%, and 2% for t = T/4, t = T/2, and t = ¾ T respectively. A comparison between predicted and measured centerline velocities yields percentage errors of 160%, 10%, and 5% at t = T/4, t = T/2, and t = ¾ T respectively. This wide error variation is apparent in Figure 4.6. The discrepancies between numerical and experimental values are significant at the beginning and end of the duty cycle.

The volume flow rates and orifice coefficents were computed, assuming a two-dimensional velocity profile for both numerical and experimental data. The differences between measured and predicted volume flow rates are given in Tables 4.2 and 4.3. Experimental data were used as reference values. Very good agreement was obtained at t = T/2, but significant errors at t = T/4 and t = ¾ T indicate that the numerical model is not reliable. It should be noted that the coarseness of the experimental data does introduce uncertainty to the accuracy of the volume flow rate calculations. Greater spatial resolution of the experimental data would allow a more accurate comparison. Orifice coefficient was calculated using Equation (4.1) in which C is the orifice coefficient, $\dot{V}$ is the volumetric flow rate, A is the orifice area, ΔP is the pressure differential, and ρ is the fluid density.

$$C = \frac{\dot{V}}{A\sqrt{\frac{2 \cdot \Delta P}{\rho}}} \tag{4.1}$$

Table 4.2: Volume flow rate (L/s).

	Predicted	Measured	Difference
t = T/4	17	9.3	83 %
t = T/2	34	35	- 4 %
t = ¾ T	13	25	- 46 %

Table 4.3: Orifice coefficient.

	Predicted	Measured	Difference
t = T/4	0.97	0.53	83 %
t = T/2	0.86	0.89	3 %
t = ¾ T	1.05	1.96	- 46 %

4.3.3. Sources of Error in the Numerical Model

There are several factors which were believed to contribute to the discrepancies between measured and computed behavior of the driven model. The most important factor is likely the discrepancy between the actual and simulated boundary conditions. Subsequent experiments (Park *et al.,* in review) have revealed that the pressure 2.5 cm upstream from the orifice varies by up to 30% in a periodic fashion. However, the numerical model utilized a steady pressure boundary condition along the upstream boundary. It is anticipated that the inclusion of a dynamic pressure boundary condition based on experimental data would greatly improve the accuracy of this model.

The moving wall boundary condition is also suspected of introducing error into the simulation. This boundary condition specifies the motion of the protrusion (see Figure 3.4). The displacement time history was obtained by measuring the orifice width as represented in high speed images of the orifice taken during the experiment. Some error is introduced by this measurement process, the limiting factor being the resolution of images produced by the camera. The orifice size varied from 0 to 17 pixels, thus introducing a 5.9% discretization error. More importantly, the identification of the orifice edge was difficult. Increased image resolution would allow a more accurate definition of the orifice edge. The errors introduced by poor image resolution may be seen in Figure 4.6 in which it appears that the orifice of the numerical model remains open for a significantly longer period than the experimental model.

Flow asymmetry is clearly noted for the experimental case as shown in Figure 4.3. However, the computational domain assumed flow symmetry about the sagittal plane (see Figure 3.1). A full simulation of the coronal plane would likely produce more accurate results.

As shown in Figure 3.3, the orifice geometry consisted of a series of straight lines which connect at sharp corners. Such corners produce extremely high gradients in the neighboring mesh, and require a very fine mesh to resolve. Unless the mesh is sufficiently fine near sharp corners, numerical errors will be introduced in these regions. However, the orifice geometry used in the numerical model was representative of the geometry of the synthetic model. A solution to this situation would be to connect straight lines with arcs of very small radii. When used in conjunction with mesh refinement, this process may mitigate the effects of sharp corners. Because of several more substantial modeling discrepancies (primarily the static instead of dynamic pressure boundary condition), such modifications were not justifiable.

Several of the modeling assumptions listed in section 3.2 may also have contributed to the discrepancies between experimental and numerical results. The three-dimensional physical model was represented in two dimensions. This does not allow the effects of turbulence to be modeled. Furthermore, no time-averaged turbulence model was used in the simulations. A laminar fluid formulation was used. Further work is needed in order to establish the contribution of time-averaged Reynolds stresses (for example a k-ε turbulence model) on the flow field.

4.4 Conclusions

Attempts were made to verify the accuracy of the flow model by comparisons with between a driven wall finite element model and experimental data. This comparison, however, did not allow a meaningful verification of the numerical model accuracy since factors such as: static instead of dynamic boundary conditions, inaccurate orifice displacement time history, two-dimensional fluid representation, and symmetric flow representation were not fully matched between the numerical and experimental configurations.

The maximum velocity attained over each cycle was predicted within 5% of the measured value. The centerline velocity was predicted within 10% for at least 65% of each period. The rate of velocity increase and decrease were accurately predicted. Qualitative characteristics of the physical model such as jet widening and narrowing were reproduced numerically. It is anticipated that verification of fluid model accuracy could be obtained with appropriate modifications to the numerical model. Specifically, wall motion should be measured more accurately and time varying pressure boundary conditions should be imposed.

5. RESULTS OF SINGLE DEGREE OF FREEDOM MODEL SIMULATIONS

Results of fluid-structure interaction simulations which utilized the single degree of freedom model introduced in Section 3.2 are presented. An analysis of typical results is given along with a discussion of the general characteristics of the model. Conclusions concerning the ability of this model to exhibit self-oscillation are made and suggestions for future work are provided.

5.1 Simulation Cases Investigated

Two parameters of the single degree-of-freedom model of Section 3.2 were varied in this study: the applied pressure differential and the model's included angle. The included angle, ψ, is defined by Scherer *et al*. (2001b) as the angle between the medial surfaces of the vocal folds. The diverging configuration is designated as a positive angle. A diagram of the included angle is shown in Figure 5.1.

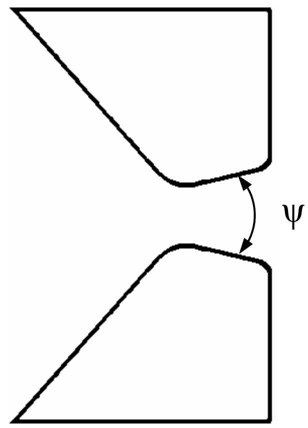

Figure 5.1: The included angle, ψ.

For each simulation, both the included angle and pressure differential were held constant. The value of the included angle ranged from -10° to 20° in 5° increments. The applied pressure differential ranged from 100 Pa to 3000 Pa. Normal human phonation usually occurs at approximately 400 Pa (Flanagan, 1972).

The results presented in this chapter were obtained for a pressure differential of 1500 Pa, and are representative of the model behavior in the ranges specified above. The behavior of the model was observed to have little dependence on included angle. For this reason, results are only shown for included angle values of -10°, 0°, and 10°.

5.2 Typical Model Response

The equilibrium position of the mass in the absence of fluid flow was designated as $x = 0$. At the time $t = 0$, the mass was subjected to fluid flow representative of that which would be obtained for an identical spring-mass system rigidly fixed at $x = 0$. The displacement time histories for included angles of -10°, 0°, and 10° and a pressure differential of 1500 Pa are shown in Figure 5.2. For all cases, fluid flow caused the model to be displaced in the negative x-direction from its initial location. The mass then vibrated about a new equilibrium point located approximately 2 mm below the original position. The vibration amplitude decayed exponentially during the time period from 0 to 0.12 seconds. After 0.12 seconds small oscillations were observed. These oscillations were on the order of 0.05 mm and were non-periodic. These are discussed further in Section 5.4.

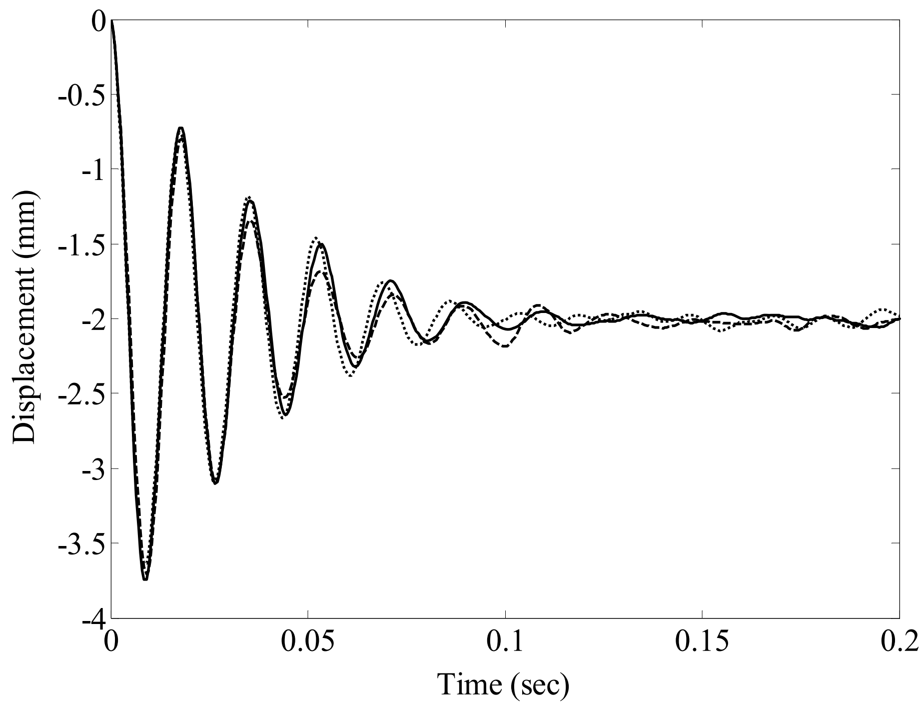

Figure 5.2: Displacement time history for three cases: ••• : $\psi = -10°$; — : $\psi = 0°$; ---: $\psi = 10°$. $\Delta P_{static} = 1500$ Pa.

5.3 Power-Flow Calculations

The transfer of energy between the fluid and structure was calculated using Newton's Second Law:

$$m\ddot{x} + c\dot{x} + kx = F_{fl} \tag{4.2}$$

Here, m is the mass, c is the damping factor, k is the spring stiffness, F_{fl} is the net fluid force, and x is the displacement. The "dot" notation indicates differentiation with respect to time. The three forces acting on the mass are F_s, the spring force, F_d, the damping force, and F_{fl}. These are given as:

$$F_s = -kx \tag{4.3}$$

$$F_d = -c\dot{x} \tag{4.4}$$

$$F_{fl} = m\ddot{x} + c\dot{x} + kx \tag{4.5}$$

The rate of energy transfer relations are:

$$P_{fl} = F_{fl}\,\dot{x} \tag{4.6}$$

$$P_{sp} = F_{sp}\,\dot{x} \tag{4.7}$$

$$P_{damp} = F_{damp}\,\dot{x} \tag{4.8}$$

where P_{fl}, P_{sp}, and P_{damp} are used to designate fluid, spring, damping power, respectively. The net work done by each force component is calculated by:

$$W_{fl} = \int_0^t P_{fl}\,dt \tag{4.9}$$

$$W_{sp} = \int_0^t P_{sp}\,dt \tag{4.10}$$

$$W_{damp} = \int_0^t P_{damp}\,dt \tag{4.11}$$

where W_{fl}, W_{sp}, and W_{damp} are used to designate fluid, spring, damping net work, respectively.

Finally, the total net work W_{tot} done by all forces was calculated using:

$$W_{tot} = \int_0^t (P_{fl} + P_s + P_d)\,dt\,. \tag{4.12}$$

5.4 Energy Transfer Analysis

There are two sources of energy transfer in this system. The net energy transferred from the fluid to the mass is referred to as "Fluid Work". The term "Damping Work" is used to indicate the net energy dissipated by the damper element. These quantities are shown as functions of time in Figures 5.3 and 5.4.

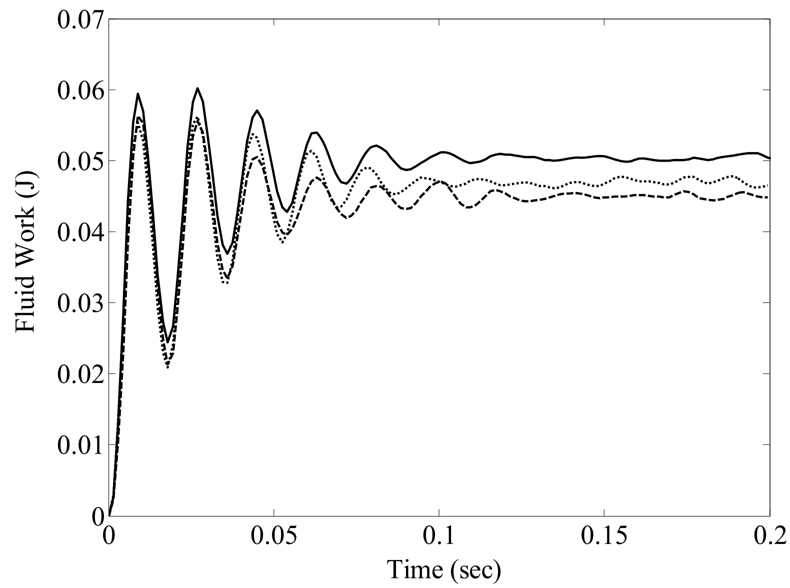

Figure 5.3: Fluid work time history for three cases: ••• : ψ = -10° ; — : ψ = 0°; --- : ψ = 10°. ΔP_{static} = 1500 Pa.

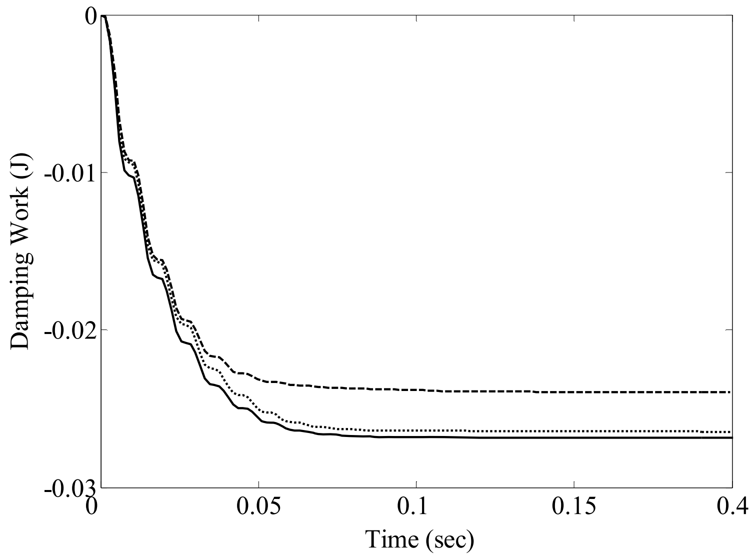

Figure 5.4: Damping work time history for three cases: ••• : ψ = -10° ; — : ψ = 0°; ---: ψ = 10°. ΔP_{static} = 1500 Pa.

As seen in figure 5.3, the total energy transferred from the fluid to the mass-spring system fluctuates initially, finally reaching a relatively stable value after t = 0.13 sec. The total energy which is dissipated by the damper is relatively constant after t = 0.13 seconds as shown in Figure 5.4. Note that for t > 0.13 sec., more total energy has been transferred to the mass than has been dissipated by the damper. This energy was converted to potential energy stored in the spring as the mass was deflected downward to its new static equilibrium.

As opposed to the behavior observed above, self-oscillation of a damped system requires that energy be continually transferred from the fluid to the structure. Thus, for a self-oscillating system, the net fluid work would exhibit a continually increasing trend rather than the static value shown for t > 0.13 seconds in Figure 5.3. Likewise, the damping work would exhibit a continually decreasing trend as the energy received from the fluid is dissipated by the damper.

5.5 Non-periodic Oscillations

Non-periodic motion of the model was observed for many simulation cases. It was hypothesized that this motion was due to small numerical fluctuations in the fluid flow solution. The $\psi = 0°$ case shown in Figure 5.5 was investigated to determine the source this motion.

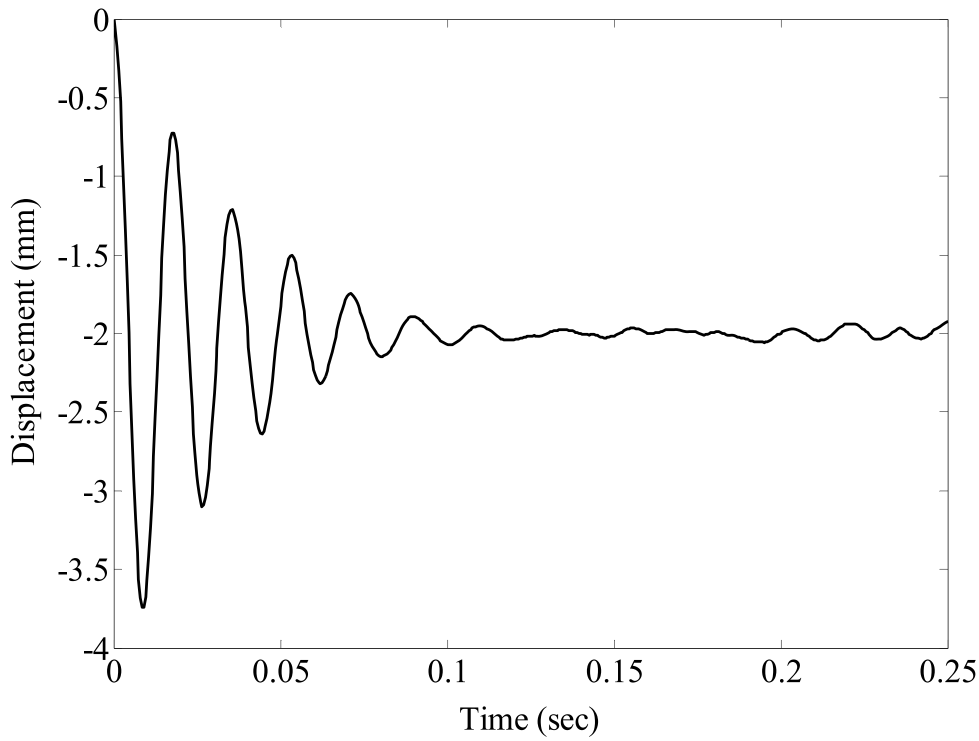

Figure 5.5: Displacement time history for the case $\psi = 0°$, $\Delta P_{static} = 1500$ Pa.

Note that oscillations apparently reappear after $t = 0.19$ sec, possibly indicating that the system is capable of self-oscillation. The amplitude of this motion was approximately 0.04 mm. The net force exerted on the mass during the time interval 0.15 to 0.25 seconds is shown in Figure 5.6. The net force acting on the mass appears to be random rather than periodic.

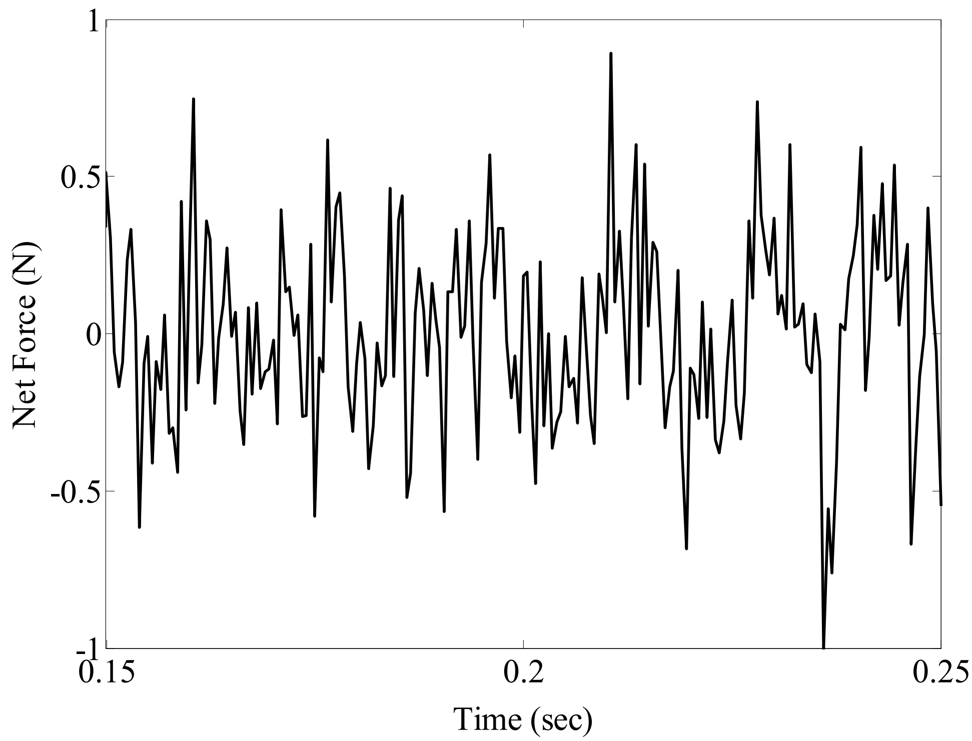

Figure 5.6: Net force acting on the mass during the time interval $0.15 < t < 0.25$ s, $\psi = 0°$, $\Delta P_{static} = 1500$ Pa

A phase-plane diagram is often used to investigate the stability of dynamic systems. Figure 5.7 shows the phase-plane diagram for the 0° included angle case for the time interval 0 to 0.25 seconds. Displacement is plotted along the abscissa and velocity is plotted along the ordinate. A phase plane diagram for the time interval 0.07 to 0.25 seconds is shown as Figure 5.8.

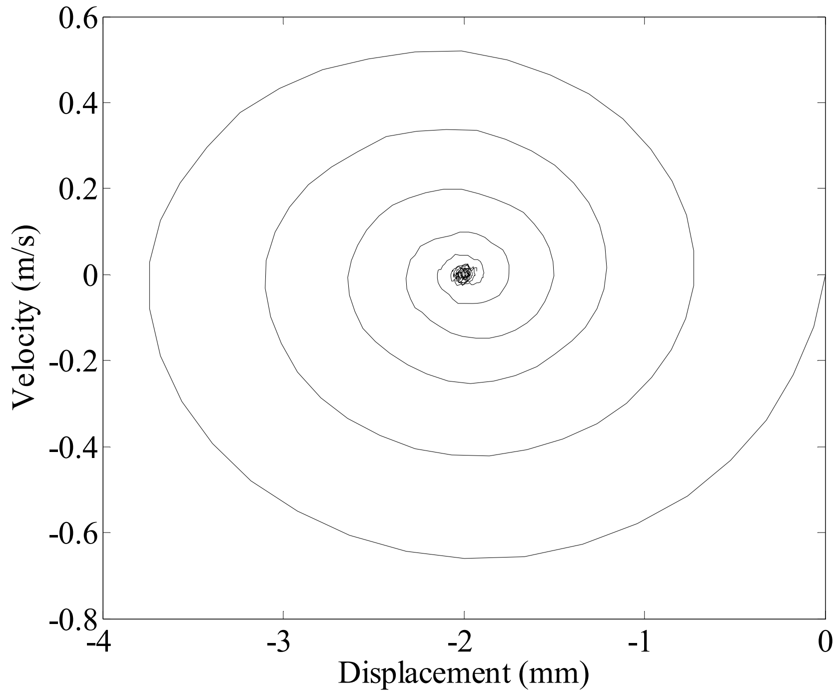

Figure 5.7: Phase plane diagram of the system response. $0 < t < 0.25$ s, $\psi = 0°$, $\Delta P_{static} = 1500$ Pa

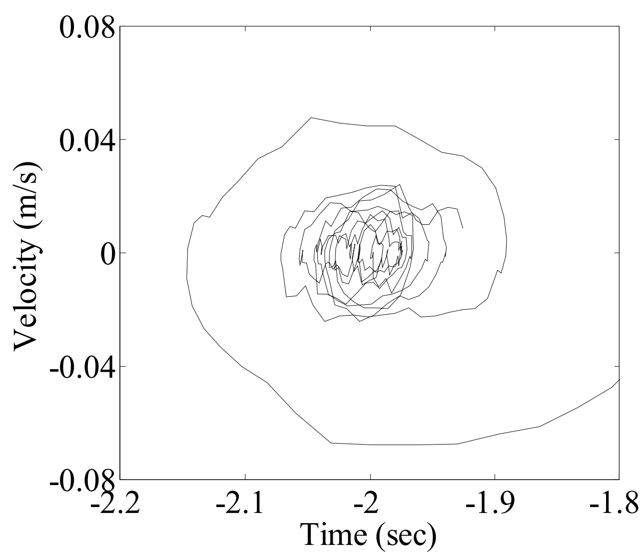

Figure 5.8: Phase plane diagram of the system response. $0.07 < t < 0.25$ s, $\psi = 0°$, ΔPstatic = 1500 Pa

As shown in Figures 5.6, and 5.8, neither the forces acting on the mass or the motion of the mass were periodic in nature. Small, random fluctuations of the fluid pressure along the top surface of the mass were also observed. It was therefore concluded that this behavior was an artifact of numerical errors rather than the product of genuine fluid-structure interactions. One possible explanation for this may be that standard SI units were used. This resulted in length scales on the order of millimeters and mass values on the order of grams. Small, numerical instabilities would have a greater effect on a system of such small scales whereas the use of the centimeter-gram-seconds system would have reduced these effects.

5.6 Conclusions

Self-oscillation of an M5 geometry, single degree-of-freedom spring-mass-damper system subjected to viscous fluid flow was investigated for included angles ranging from -10° to 20° under static pressure loading conditions ranging from 100 to 3000 Pa. Self-oscillation was not observed for any cases in the stated ranges.

Previously reported single degree-of-freedom models have exhibited self-oscillation. The single mass model of Flanagan and Landgraf (1968) utilized a single spring-mass damper system subjected to ideal fluid flow and acoustic loading. In contrast, the current model was subjected to viscous fluid flow in the absence of acoustic loading. It may be hypothesized from this result that viscous fluid forces play a less important role in self-oscillation than compressibility effects. A study by Thomson (2004) compared the relative magnitude of viscous and normal pressure forces in a numerical, self-oscillating continuum model of the human vocal folds. He concluded that the viscous shear forces were insignificant in comparison to the normal pressure forces. However, a Navier-Stokes fluid formulation will naturally predict surface pressures more accurately than Bernoulli's equation. Also, a Navier-Stokes model is capable of predicting flow structures such as vortex formation and separation point.

The two-mass model of Ishizaka and Flanagan (1972) has also been shown to exhibit self-oscillation in the absence of acoustic loading. This behavior is attributed to the converging/diverging nozzle configuration obtained as the two masses move out of phase with each other. The fluid flow separation point moves back and forth in the inferior/superior direction as a result of this motion. The pressure forces produced by the temporal asymmetry in the time history of the orifice coefficient cause self-oscillation of the two-mass model. Although the current model relied upon a much more advanced viscous flow model, the presence of viscous forces, vortices, and other flow structures were not sufficient to induce self-oscillation. One plausible explanation for the observed behavior is that structural complexity, in particular a time varying orifice shape, is a requirement for self oscillation.

6. MODAL ANALYSIS RESULTS

In this chapter, the results of modal analyses of vocal fold models are presented. A verification study was performed to ensure that the results obtained via Ritz Method and finite element method modal analyses were identical. A geometric sensitivity study was performed to determine the sensitivity of modal frequencies to changes in model length, width, and thickness. The role of transverse displacements in modal behavior was investigated.

6.1 Verification Study

In order to verify the Ritz and ADINA methods, a comparison study was conducted. The continuum model geometry and boundary conditions shown in Figure 2.1 were used. An isotropic, rather than transversely isotropic material was used because of a lack of information regarding the longitudinal Young's modulus. The isotropy ratio, n, indicates the level of anisotropy in a substance and is defined as the ratio of the transverse to longitudinal Young's moduli:

$$n = E_{trans}/E_{long}\,. \tag{6.1}$$

To the author's knowledge, neither E_{long} nor the isotropy ratio has been measured for human vocal fold tissue. Berry & Titze (1996) assumed that the y-displacement function, $\psi(x,y,z,t)$ was zero. This effectively removes the longitudinal Young's modulus from the stiffness matrix [**C**]. While this approach is possible when using the Ritz Method, the finite element program used in this study requires a numerical value for the longitudinal Young's modulus. The use of an isotropic material allowed a consistent comparison to be made. The material was also assumed to be completely compressible in order to avoid adverse effects caused by transverse stresses which are discussed in Section 6.4. The material properties used in the verification study are given in Table 6.1.

Table 6.1: Tissue properties for the verification study.

	CGM Units	SI Units
Young's modulus, E	10^5 dyne/cm^2	10^4 Pa
Density, ρ	1.03 g/cm^3	1030 kg/m^3
Poisson's ratio, ν	0	0

Anterior/posterior constraints were applied to the finite element model to reproduce those implicitly used in the Ritz method. The results are presented in Table 6.2. The agreement between computed natural frequencies suggests that the numerical procedures have been correctly implemented.

Table 6.2: Comparison of modal analysis results.

Mode	Resonance Frequency (Hz)		Difference
	Ritz	ADINA	
1	133	133	0.0%
2	151	151	0.0%
3	160	160	0.0%
4	227	227	0.0%
5	239	238	0.2%

6.1.1. Comparisons with Previous Results

Modal analysis via the Ritz Method was performed using the continuum model of Figure 2.1 and the transversely isotropic material properties given in Table 3.2. The first five mode shapes and modal frequencies are shown in Figure 6.1. These mode shapes and frequencies were found to be identical to those presented by Berry and Titze (1996).

Mode 1: 133 Hz

Mode 2: 151 Hz

Mode 3: 153 Hz

Mode 4: 194 Hz

Mode 5: 220 Hz

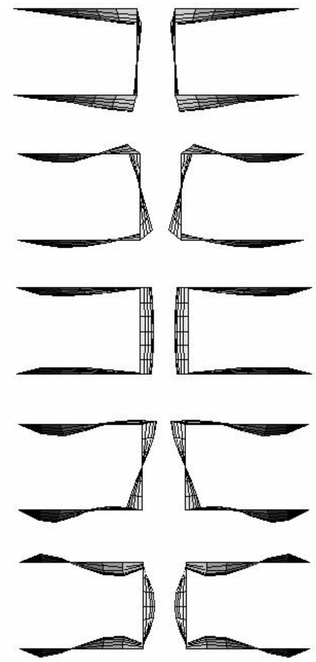

Figure 6.1: Modal frequencies and mode shapes of the first five modes obtained via the Ritz Method. Mode shapes are as viewed as coronal cross-sections.

6.2 Geometric Sensitivity of the Continuum Model

Using the above model and system parameters, a geometric sensitivity study was performed. The thickness, depth, and length of the continuum model were varied independently. The relative changes of the first five modal frequencies were calculated as a function of the relative changes in each dimension. Relative changes in frequency are shown in Figures 6.2, 6.3, and 6.4. Note that the scale is the same for each figure to facilitate direct comparisons. For reference, modal frequency as a function of thickness, depth, and length are shown in Appendix B.

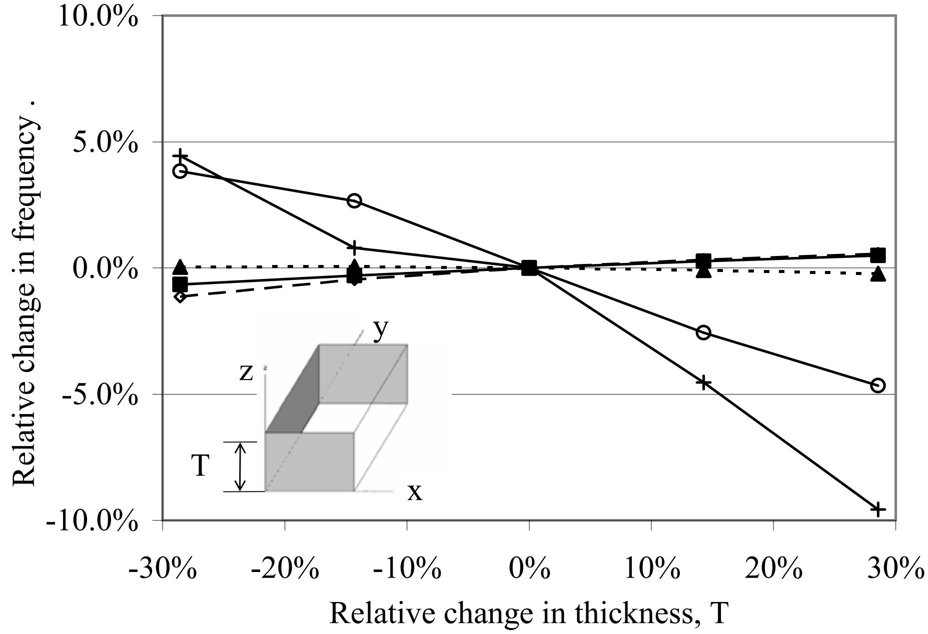

Figure 6.2: Sensitivity of modal frequencies to changes in thickness, T.
■ : Mode 1; ◊ : Mode 2; ▲ : Mode 3; ○ : Mode 4; + : Mode 5.

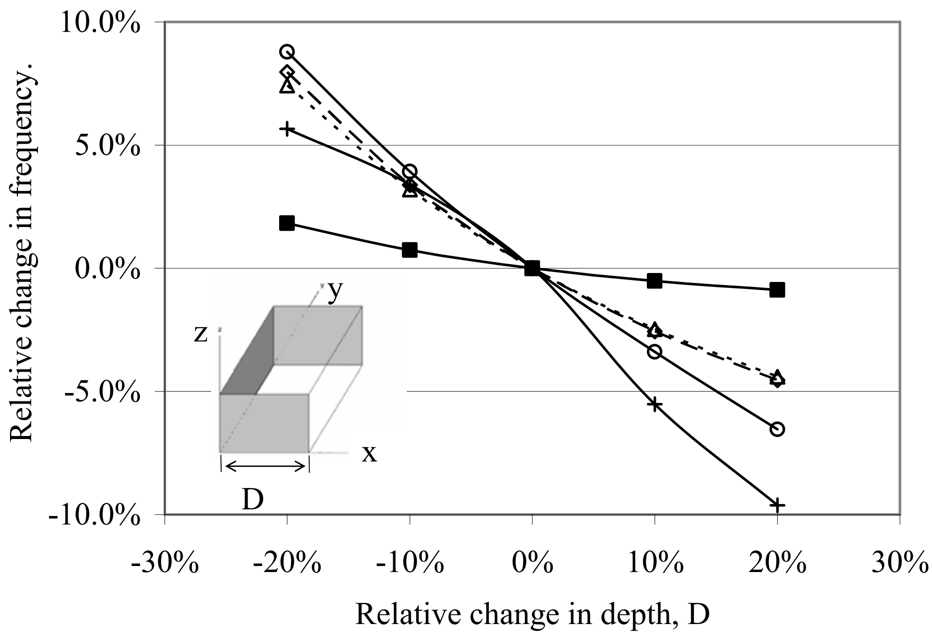

Figure 6.3: Sensitivity of modal frequencies to changes in depth, D.
■ : Mode 1; ◊ : Mode 2; ▲ : Mode 3; ○ : Mode 4; + : Mode 5.

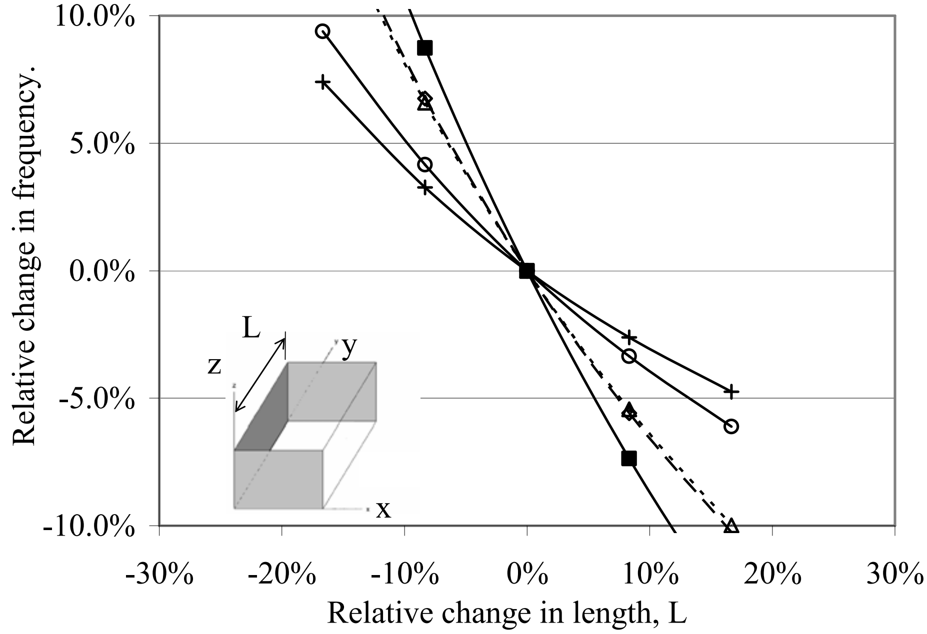

Figure 6.4: Sensitivity of modal frequencies to changes in length, L.
■ : Mode 1; ◊ : Mode 2; ▲ : Mode 3; ○ : Mode 4; + : Mode 5.

The modal frequencies are least sensitive to changes in thickness, T. As shown in Figure 6.2, the first, second, and third modal frequencies are nearly constant with changes in thickness, while the fourth and fifth modal frequencies decrease slightly as thickness is increased.

The model is significantly more sensitive to changes in depth, D, than to changes in thickness as shown by a comparison between Figures 6.2 and 6.3. The first modal frequency decreases gradually with increasing depth. The second, third, and fourth modal frequencies decrease at a slightly higher rate.

Finally, the model is most sensitive to changes in length, L as shown in Figure 6.4. The first modal frequency decreases very sharply with increased length while the second and third modal frequencies decrease at a slightly lower rate. The fourth and fifth modal frequencies also decline sharply. In fact, one may note that the least sensitive mode in Fig 6.4 declines more sharply than any of the modes in Figures 6.2 or 6.3.

Previous studies have reported that most of the vibratory energy is found within the first three modes of vibration (Alipour *et al*., 2001, Berry *et al*. 2001). Hence, it has been proposed that these modes are critical to the self-oscillation of the vocal folds. The fourth and fifth modes may also be important in voice production since they occur near the first resonance of the vocal tract, thus contributing significantly to radiated sound.

6.3 Range of Validity of Two-Dimensional Models

Figure 6.5 shows the first five modal frequencies as a function of length over a wide range of length values.

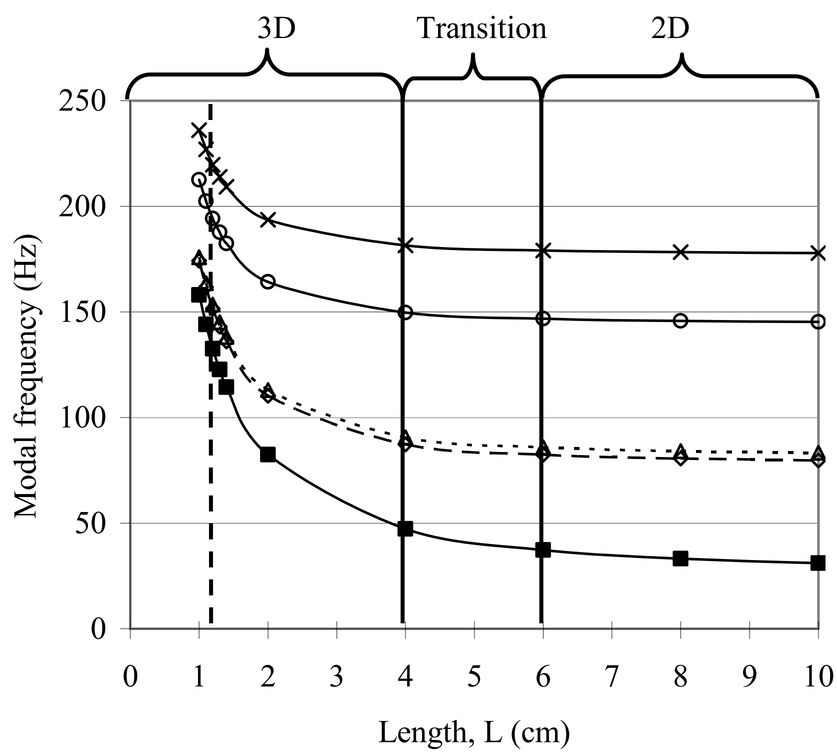

Figure 6.5: Modal frequency versus model length. L. The nominal length is designated by a dashed line. ■ : Mode 1; ◊ : Mode 2; ▲ : Mode 3; ○ : Mode 4; x : Mode 5.

Three distinct regions can be identified in Figure 6.5. The modal frequencies are highly dependent on length in the region from zero to four centimeters. This is identified as the three-dimensional region. The other two dimensions are depth and thickness. A transitional region of moderate dependence on length exists from about four to six centimeters. As the length of the continuum model exceeds six centimeters, the resonance frequencies become insensitive to changes in length, indicating two-dimensional behavior. In this region, the continuum behaves as an infinitely long rather than a finite parallelepiped. Simulations of a two-dimensional model yield modal frequencies which are identical to those obtained for an extremely long ($L = 10^9$ cm) model. The continuum model (which is representative of human vocal folds) has a nominal length of 1.2 cm, clearly within the three-dimensional region.

This three-dimensional behavior is a direct result of shear and normal stresses which act on the transverse (xz) plane. Two-dimensional plane strain models do not account for these "out-of-plane" stresses. As seen in Figure 6.5, these stresses have a dramatic influence of the vibratory behavior of this vocal fold model. This suggests that the vocal folds themselves may be inherently three-dimensional in nature. As a consequence, models which do not account for these effects may be in error.

6.4 The Influence of Transverse Stresses

A very long structure may be effectively modeled in two dimensions with very high accuracy in the regions not significantly affected by end effects. One assumption which is used in modeling such structures is the plane strain assumption: strains (and therefore displacements) in the transverse direction are assumed to be zero. Similarly, the transverse displacement function was assumed to be zero in the Ritz Method formulation of the continuum model. However, plane strain was not explicitly assumed because the continuum model is based on a three-dimensional formulation of Hooke's Law. However, suppression of motion in the y-direction may cause significant errors.

To investigate the influence of transverse displacement constraints, a comparison was made between cases in which the motion in the y-direction was constrained and unconstrained. The finite element method was used to perform the modal analysis. An isotropic material was used for the reasons already stated in Section 6.1. The vocal fold tissue was assumed to be incompressible. The material was defined using the material properties listed in Table 6.3.

Table 6.3: Tissue properties for the isotropic case.

	CGM Units	SI Units
Young's modulus, *E*	10^5 dyne/cm^2	10^4 Pa
Density, ρ	1.03 g/cm^3	1030 kg/m^3
Poisson's ratio, ν	0.4999	0.4999

The rectangular domain was meshed using 840 quadratic (27 node) three-dimensional solid finite elements for a total of 7875 nodal points. Repeated calculations using varying mesh densities confirmed that this configuration represents a mesh-converged solution. The model geometry and boundary conditions were consistent with previous cases.

For constrained cases, all finite element nodes (except those on the fixed boundaries) were constrained to move within the XZ plane. For unconstrained cases, all interior and free surface nodes were allowed to move in all three directions.

The displacement fields were obtained along a plane located 0.3 cm from the front face at one-quarter the total length of the model, as illustrated in Figure 6.6.

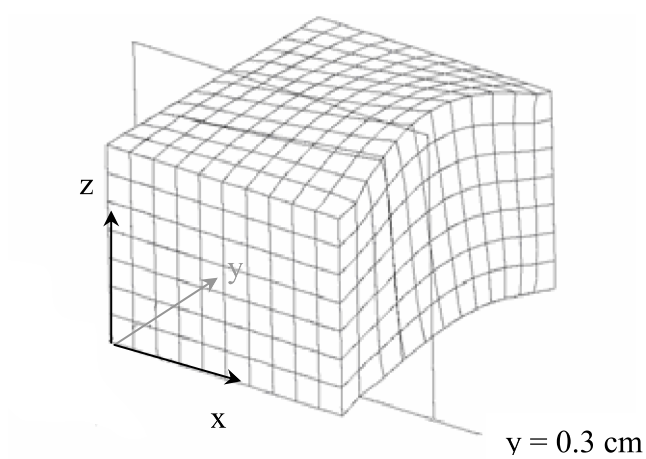

Figure 6.6: Sketch of the first mode shape and the plane y = 0.3 cm.

The displacement fields for constrained and unconstrained cases at the plane y = 0.3 cm are shown in Figure 6.7. Although the maximum displacements computed are not identical, there is very little quantitative or qualitative difference between the two displacement fields.

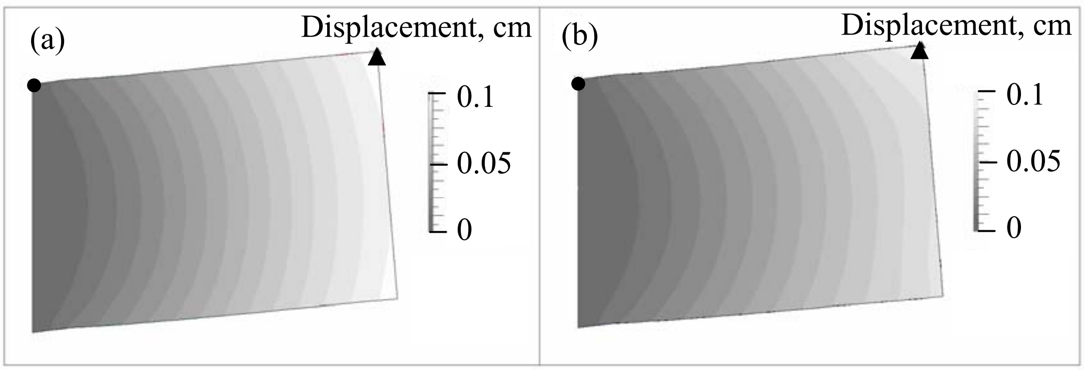

Figure 6.7: Displacement field results along y = 0.3 cm:
(a) constrained; Maximum: ▲0.097 cm; Minimum: ● 0.0 cm
(b) unconstrained; Maximum: ▲0.104 cm; Minimum: ● 0.0 cm

The stresses normal to the y = 0.3 cm plane, σ_{yy}, are shown in Figure 6.8. The effects of constraint forces required to prevent motion in the y-direction are clearly visible in Figure 6.8 (a). The difference between the constrained and unconstrained cases are qualitatively and quantitatively different. In the unconstrained case, maximum and minimum stress levels are obtained at the boundaries (as would be expected) and are on the order of 7 kPa. In contrast, the maximum and minimum stress levels in the constrained case occur at the medial surface. The maximum stress levels in the constrained case are on the order of 80 kPa – one order of magnitude greater than in the unconstrained case.

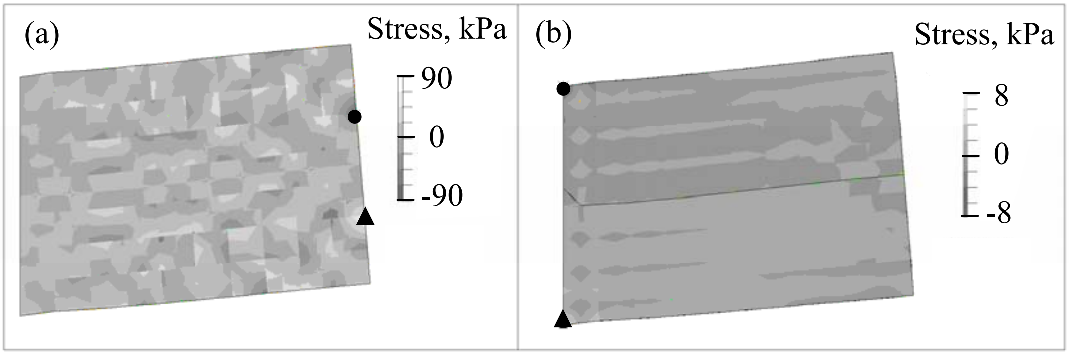

Figure 6.8: σ_{yy} stress fields at the plane y = 0.3 cm:
(a) constrained case; Maximum: ▲75.8 kPa; Minimum: ● -75.8 kPa
(b) unconstrained case; Maximum: ▲6.78 kPa; Minimum: ● -6.78 kPa

The modal frequencies also differ between the constrained and unconstrained cases. Table 6.4 lists the first six mode shapes and modal frequencies for both cases. Arrows are used to identify similar mode shapes which occur in both cases. For example, mode 2 in the unconstrained case has the same basic shape as mode 3 in the constrained case.

Table 6.4: Frequencies and mode shapes for constrained and unconstrained cases.

	Constrained		Unconstrained		
	(Hz)	Mode Shape	Mode Shape	Frequency (Hz)	% Difference
Mode 1	81			73	11%
Mode 2	117			113	6%
Mode 3	120			115	2%
Mode 4	153			131	16%
Mode 5	175			144	23%
Mode 6	177			150	---

For a given mode shape, the presence of constraints resulted in consistently greater modal frequencies than those obtained in the absence of constraints. This is a consequence of the constraint forces which artificially stiffen the structure. The relative differences between constrained and unconstrained modal frequencies are listed in Table 6.4, with the unconstrained case as the reference value. The relative difference varies between 2% and 23%. The second and third modal frequencies are relatively similar; the fourth and fifth modes exhibit greater discrepancies. Unfortunately there seems to be no consistent trend in the differences between constrained and unconstrained modes.

6.5 Conclusions

The resonance frequencies of the vocal folds model were found to be most sensitive to changes in length. The results provided in Figure 6.5 imply that a two-dimensional model constructed using standard tissue parameters will exhibit modal frequencies much lower than expected. This phenomenon has been reported by Thomson

(2004) and may be explained by the fact that two-dimensional planar strain models neglect to correctly model the out of plane shear and normal stresses. These observations suggest that the vibration of the human vocal folds may also be influenced by similar out of plane stresses. More detailed analytic models may be used in conjunction with experiments to test this hypothesis. The relative contribution of shear versus normal out of plane stresses may also be of interest in order to simplify future models.

The suppression of lateral motion in an isotropic continuum model of the vocal folds introduces errors in the calculation of mode shapes and modal frequencies. The modal frequencies obtained in a constrained case are always greater than those obtained in the unconstrained case. In general, the discrepancies between modal frequencies in each case are greater for increasingly higher mode numbers. These observations suggest that hybrid models may be biased due to the artificial stiffening caused by anterior/posterior constraints. While this effect is noticeable in linear, small amplitude analysis, it may be more pronounced during the large amplitude oscillations encountered in phonation. Unfortunately, the magnitude of such errors cannot be predicted other than by the construction and analysis of an unconstrained model of identical characteristics.

The results of Section 6.4 were obtained using an isotropic rather than a transversely isotropic material. Because vocal fold muscle fibers are oriented in the longitudinal direction, the vocal fold tissue is most accurately modeled as a transversely isotropic material. However, there is no available data for many tissue properties in the transverse plane. Many existing vocal fold models (Berry and Titze, 1996, Alipour *et al.*, 2001) assume that no displacement occurs in the longitudinal direction. It has been shown in this study that this constraint would artificially stiffen an isotropic structure. The effect of this assumption on transversely isotropic cases has not yet been investigated. It is suggested that a parametric study be conducted in which the isotropy ratio, n, is varied to account for the unknown tissue properties.

Finally, because the above models differ from the human vocal folds in many aspects (e.g. geometry, material properties, and boundary conditions), the results presented above are not directly applicable to the human vocal folds. However, the results suggest that three-dimensional stresses may have a significant influence on the vibratory characteristics of the human vocal folds.

7. CONCLUSIONS

7.1 Summary

Numerical simulations of the synthetic model were presented in Chapter 4. The numerical model predicted fluid behavior which was observed to exhibit qualitative similarities to the synthetic model. The maximum velocity magnitude for each cycle was predicted reliably, but significant errors were observed during opening and closing portions of the oscillation cycle. Several likely sources of error were identified. Primary sources of error included the lack of dynamic boundary conditions, inaccurate orifice displacement time history, and the symmetric flow assumption.

The behavior of a lumped mass model subjected to viscous fluid flow was presented in Chapter 5. This model was not observed to exhibit self oscillation. These results suggest that the modeling of viscous forces and flow structures such as separation point and vortex formation are not sufficient to induce self-oscillation of a rigid single mass model.

Modal analysis results were presented in Chapter 6. The modal properties of the nominal continuum model were observed to be affected by out of plane stresses. This observation explains some of the difficulties reported by Thomson (2004) in modeling the vocal fold structure in two dimensions. Two dimensional models (and some hybrid models) are not capable of modeling these out of plane stresses and will thus be unable to simulate the effects of out of plane stresses.

7.2 Recommendations for Future Research

Numerical simulations of the driven physical model may be useful in determining the contribution of viscous forces, compressibility and turbulence in fluid flows representative of human phonation. Subsequent simulations should include dynamic boundary conditions and rounded corners. An accurate determination of the orifice motion is also critical. Significantly more accurate results are expected as these error sources are appropriately addressed. Following full verification of the finite element code accuracy, similar simulations may also be useful in quantitatively evaluating the contribution of unsteady terms in the Navier-Stokes equations. Such a study would provide an numerical verification of the quasi-steady assumption. A more complete understanding of these various fluid effects will aid in the creation of more accurate reduced order models of human phonation.

The single mass model of Chapter 5 was constructed specifically to investigate the influence of viscous flow on self-oscillation. As a consequence, several mechanisms believed to contribute to the self-oscillation were not examined in this study. These include acoustic loading, and structural complexity. Instead of attempting to design a simple self-oscillating model, a suggested approach would be to instead examine a model which is capable of self-oscillation. Various fluid and structural aspects could then be modified independently to observe which mechanisms (such as those mentioned above) are most essential to self-oscillation. Numerical models may be used to isolate variables in ways which cannot be duplicated in the laboratory.

The continuum model utilized in Chapter 6 represents an idealized model of the human vocal folds. New geometric data should be utilized to create a model more geometrically similar to the human vocal folds. Layers should also be added to this model as more tissue parameters become available. Until the time that all tissue parameters are known, parametric studies of the role of various tissue properties may be used. These may become indispensable because of the natural variation of tissue parameters in actual vocal fold tissues. Numerical studies should also be referenced to experimental studies in order to determine if and how the human vocal folds are affected by out of plane stresses. Finally, all modal analyses performed to date have assumed that the vocal folds to be in an initially stress-free configuration. In reality, posturing of the vocal folds occurs prior to phonation. This introduces unknown stresses to the vocal fold structure. The presence of these stresses may change the qualitative as well as quantitative behavior of the vocal folds. The effects of posturing on modal properties should be examined in future research.

REFERENCES

LIST OF REFERENCES

ADINA Theory and Modeling Guide Volume I, 2004, ADINA System Online Manuals, ADINA R&D Inc., Watertown, MA 02472, pp. 516.

ADINA Theory and Modeling Guide Volume III, 2004, ADINA System Online Manuals, ADINA R&D Inc., Watertown, MA 02472, pp. 115-118.

Alipour F., Berry D., and Titze I.R., 2000, "A finite-element model of vocal-fold vibration," *J. Acoust. Soc. Am.* **108**, pp. 3003–3012.

Alipour-Haghighi, F., and Titze, I. R., 1991, ''Elastic models of vocal fold tissues,'' *J. Acoust. Soc. Am.* **90**, pp.1326–1331.

Baer T., 1981, "Investigation of the phonatory mechanism," *Am. Speech and Hearing Assoc. Reports* **11** pp. 38–46.

Bathe, J.K., 1996, *Finite Element Procedures*, Upper Saddle River, New Jersey: Prentice Hall.

Berry, D.A., 2001, "Mechanisms of modal and nonmodal phonation," *J. Phonetics* **29** pp. 431-450.

Berry, D.A., Montequin D.W., and Tayama, N., 2001, "High-speed digital imaging of the medial surface of the vocal folds," *J. Acoust. Soc. Am.* **110**, pp. 2539–2547.

Berry, D.A., and Titze, I.R., 1996, "Normal modes in a continuum model of vocal fold tissues," *J. Acoust. Soc. Am.* **100**, pp. 3345–3354.

Berry, D.A., Clark, M.J.O., Montequin, D.W., and Titze, I.R., 2001 "Characterization of the medial surface of the vocal folds", *Ann. Otol. Rhinol. Laryngol.* **110** (5), pp. 470-477.

Chan, R.W., and Titze, I.R., 1999, "Viscoelastic shear properties of the human vocal fold mucosa: measurement methodolgy and empirical results", *J. Acoust. Soc. Am.* **106**, pp.2008-2021.

Cook, R.D., Malkus, D.S., Plesha, M.E., and Witt, R.J., 2001, *Concepts and Applications of Finite Element Analysis*, 4th Edition, Wiley and Sons Inc.

de Vries, M.P., Schutte, H.K., and Verkerke, G.J., 1999, "Determination of parameters for lumped parameter models of the vocal folds using a finite-element method approach," *J. Acoust. Soc. Am.* **106,** pp. 3620-3628.

Flanagan, J.L., Landgraf, L.L., 1968, "Self-oscillating source for vocal tract synthesizers", *IEEE Trans. On Audio and Electroacoustics*, **AU-16**, No. 1, pp. 57-64.

Flanagan, J. L., 1972, *Speech Analysis, Synthesis, and Perception*, 2nd edition, Springer-Verlag, New York.

Fox, R.W., MacDonald, A.T., and Pritchard, P.J., 2003, *Introduction to Fluids Mechanics*, 6th Ed., John Wiley & Sons Inc.

Grey, H., 1918, *Anatomy of the Human Body*, XI. Splanchnology, 1a. Figure 954. Available at http://www.bartleby.com/107/236.html (as of November 2005).

Gunter, H., 2003, "A mechanical model of vocal-fold collision with high spatial and temporal resolution," *J. Acoust. Soc. Am.* **113,** pp. 994-1000.

Hirano, M., and Bless, D.M., 1993, *Videostroboscopic Examination of the Larynx*, San Diego, Singular Publishing Group.

Hirano, M., and Sato, K., 1993, *Histological Color Atlas of the Human Larynx*, San Diego, Calif., Singular Pub. Group.

Horacek. J., and Svec, J.G., 2002a "Aeroelastic model of vocal-fold-shaped vibrating element for studying the phonation threshold," *J. of Fluids and Structures* **16**, pp. 931-955.

Horacek J., and Svec, J.G., 2002b, "Instability boundaries of a vocal fold modelled as a flexibly supported rigid body vibrating in a channel conveying fluid", *Proceedings of IMECE 2002*, pp. 1-12.

Hunter, E.J., Titze, I.R., and Alipour, F., 2004 "A three-dimensional model of vocal fold abduction/adduction," *J. Acoust. Soc. Am.* **115**, pp. 1747-1759.

Titze, I.R., Story, B.H., 2002, "Rules for controlling low-dimensional vocal fold models with muscle activation," *J. Acoust. Soc. Am.* **112** (3), pp. 1064–1076.

Ishizaka, K., and Flanagan, J.L., 1972 "Synthesis of voiced sounds from a two-mass model of the vocal cords," *Bell Syst. Tech. J.* **51** pp. 1233–1267.

Jiang, J.J., Shah, A.G., Hess, M.M., Verdolini, K., Banzali, F.M., and Hanson, D.G., 2001, "Vocal fold impact stress analysis," *Journal of Voice* **15** (1) pp. 4-14.

Jiang, J.J., and Titze, I.R., 1993, "A methodological study of hemilaryngeal phonation," *Larygoscope* **103**, pp. 872-882.

Jiang, J.J., and Titze, I.R., 1994, "Measurement of vocal fold intraglottal pressure and impact stress," *Journal of Voice* **8**, pp, 132-144.

Kob, M., 2002, *Physical Modeling of the Singing Voice*, Ph.D. Dissertation, University of Technology Aachen. Logos-Verlag, Berlin.

LaMar, M.D., Qi, Y., and Xin, J., 2003, "Modeling vocal fold motion with a hydrodynamic semicontinuum model," *J. Acoust. Soc. Am.* **114** pp. 455-464.

Larsen, C.R., 2002, "How the Larynx (Voice Box) Works," Center for Voice at Northwestern Website available at www.voice.northwestern.edu/howworks.html, (as of November, 2005).

Leissa, A., and Zhang, Z.D., 1983, 1983, “On the three-dimensional vibrations of the cantilevered rectangular parallelepiped,” *J. Acoust. Soc. Am.* **73** pp. 2013–2021.

Lucero, J.C., 1999, “A theoretical study of the hysteresis phenomenon at vocal fold oscillation onset-offset,” *J. Acoust. Soc. Am.* **105** (1), pp 423-31.

Lucero, J.C., 2004, "Dynamics of Vocal Fold Oscillation", Invited Plenary Talk XXVII Nat. Cong. App. & Comp. Math.

Meirovitch, L., 2000, *Principles and Techniques of Vibrations*, Prentice-Hall, Upper Saddle River, New Jersey..

Min, Y.B., Titze, I.R., and Alipour-Haghighi, F., 1995, "Stress-strain response of the human vocal ligament", *Ann. Otol. Rhinol. Laryngol.* **104**, pp. 563-569.

National Aeronautics Space Administration, 1995, *Man-Systems Integration Standards Revision B*, Vol. 1, Section 3.1.2.

Neubauer, J., Mergell, P., Eysholdt, U., and Herzel, H., 2001, “Spatio-temporal analysis of irregular vocal fold oscillations: Biphonation due to desynchronization of spatial modes,” *J. Acoust. Soc. Am.* **110**, pp. 3179-3192.

Park, J.B., and Mongeau, L., in review, “Instantaneous orifice discharge coefficient measurements of a physical, driven model of the human larynx,” J. Acoust. Soc. Am.

Pillai, R.S., Chandra, T., Miller, I.F., Lloyd-Still, J., and Yeates, D.B., 1992, "Work of adhesion of respiratory tract mucus", *J. Appl. Physiol.* **72** (4), 1604-1610.

Ritz, W., 1908, “U ber eine neue Methode zuer Lo¨sung gewisser Variations problemeder mathematischen Physik,” *Z. Reine Angew. Math.* **135,** pp. 1–61.

Rosa, M.O., Pereira, J.C., Grellet, M., and Alwan, A., 2003, "A contribution to simulating a three-dimensional larynx model using the finite element method," *J. Acoust. Soc. Am.* **114** (5), pp. 2893-2905.

Roy, N., Merrill, R., Thibeault, S.,Gray, S., and Smith, E., 2004, “Voice disorders in teachers and the general population: Effects on work performance, attendance, and future career choices,” *J. of Speech, Lang. and Hear. Res.* **47**(3), 542—551.

Saito, S., Fukuda, H., and Kitahira, S., 1985 “Pellet tracking in the vocal fold while phonating: experimental study using canine larynges with muscle activity,” In *Vocal Fold Physiology*, Denver: Denver Center for the Performing Arts.

Scherer, R., and Titze, I.R. 1983, “Pressure-flow relationships in a model of the laryngeal airway with a diverging glottis,” In *Vocal Fold Physiology: Contemporary research and clinical issues*, College-Hill Press, San Diego CA., pp. 179-193.

Scherer, R.C., De Witt, K.J., and Kucinschi, B.R., 2001 a, "The effect of exit radii on intraglottal pressure distributions in the convergent glottis.", *J. Acoust. Soc. Am.* **110** (5), pp. 2267-2270.

Scherer, R.C., Shinwari, D., De Witt, K.J., Zhang, C., Kucinschi, B.R., and Afjeh, A.A., 2001 b, "Intraglottal pressure profiles for a symmetric and oblique glottis with a divergence angle of 10 degrees", *J. Acoust. Soc. Am.* **109** (4), pp. 1616-1630.

Scherer, R.C., Shinwari, D., De Witt, K.J., Zhang, C., Kucinschi, B.R., and Afjeh, A.A., 2002, "Intraglottal pressure distributions for a symmetric and oblique glottis with a uniform duct", *J. Acoust. Soc. Am.*, **112** (4), pp. 1253-1261.

Selbie, W.S., Gewalt, S.L., and Ludlow, C.L., 2002, "Developing an anatomical model of the human lanryngeal cartilages from magnetic resonace imaging", *J. Acoust. Soc. Am.* **112**, (3), pp. 1077-1090.

Sidlof, P., Svec, J.G., Horacek, J., Vesely, J., Klepacek, I., and Havalik, R., 2004, "Determination of vocal fold geometry from excised laryges: Methodology and preliminary results", *2004 Int. Conf. on Voice Physiology and Biomechanics*.

Smith, E., Gray S.D., Dove, H., Kerchner, L., Heran, H., , 1998, “Frequency and effect of teachers voice problems,” *Journal of Voice* **11**, pp. 81-87.

Svec, J.G., Horácek, J., Sram, F., and Vesely, J., 2000, “Resonance properties of the vocal folds: In vivo laryngoscopic investigation of the externally excited laryngeal vibrations,” *J. Acoust. Soc. Am.* **108**, pp. 1397-1407.

Svec, J.G., 2002, “Research journey: chest-falsetto discontinuity and videokymography,” First International Conference on the Physiology and Acoustics of Singing (PAS1) October 3-5, 2002, Groningen, the Netherlands

Tayama, N., Chan, R.W., Kaga, K., and Titze, I.R., 2002, “Functional definitions of vocal fold geometry for laryngeal biomechanical modeling,” *Ann Otol Rhinol Laryngol.* **111**(1), pp.83-92.

Thomson, S.L., 2004, *Fluid-Structure Interactions Within the Human Larynx* Ph.D. Dissertation, Purdue University.

Thomson, S.L., Mongeau, L., and Frankel, S.H., 2005, "Aerodynamic transfer of energy to the vocal folds", *J. Acoust. Soc. Am.*, 118 (3) pp. 1689-1700

Titze, I.R., and Strong, W.J., 1975, “Normal modes in vocal cord tissues,” *J. Acoust. Soc. Am.* **57**, pp. 736–744.

Titze, I.R., and Talkin D., 1979, “A theoretical study of the effects of various laryngeal configurations on the acoustics of phonation,” *J. Acoust. Soc. Am.* **66**, pp. 60-74.

Titze, I.R., 1988, “The physics of small-amplitude oscillation of the vocal folds,” *J. Acoust. Soc. Am.* **83**, pp. 1536-1552.

Titze, I.R. 2002, “Regulating glottal airflow in phonation: Application of the maximum power transfer theorem to a low dimensional phonation model,” *J. Acoust. Soc. Am.* **111**, (1), pp. 367-376.

Titze, I.R., 1976, "On the mechanics of vocal-fold vibration", *J. Acoust. Soc. Am.* **60** (6), pp.1366-1380.

Titze, I.R., and Hunter, E.J., 2004, "Normal vibration frequencies of the vocal ligament", *J. Acoust. Soc. Am.* **115** (5), pp.2264-2269.

Trevisan, M.A., Eguia, M.C., and Mindlin, G.B., 2001, "Nonlinear aspects of analysis and synthesis of speech time series data", *Phy. Rev. E*, **63,** pp. 1-6.

Verdolini, K., and Ramig, L.O., 2001, "Occupational risks for voice problems," *Journal of Logopedics, Phoniatrics, Vocology*. **26** (1) pp.37-46.

Washizu, K., 1968, *Variational Methods in Elasticity and Plasticity*, New York: Pergamon; pp. 43–44.

Zhang, K., Chan, R.W., and Siegmund, T., (in review), "Constitutive characterization of tensile deformation of the human vocal fold cover with applications to fundamental frequency regulation".

Zhang, Z., Mongeau, L., and Frankel, S.H., 2002, "Experimental verification of the quasi-steady assumption approximation for aerodynamic sound generation by pulsating jets in tubes", *J. Acoust. Soc. Am*, **112**, (4), pp. 1652-1663.

Zhao, W., Zhang, C., Frankel, S.H., and Mongeau, L., 2002, "Computational aeroacoustics of phonation, part I: numerical methods, acoustic analogy validation, and effects of glottal geometry," *J. Acoust. Soc. Am.* **112**, (5), pp. 2134-2146.

APPENDIX

Appendix A: Description of Driven Model Experimental Apparatus

A.1 Synthetic Model of the Vocal Folds

A physical model of the human vocal folds was constructed by Park et al., (2005). A silicone rubber compound was used to create a model geometrically similar to the human vocal folds. This model was subjected to forced oscillations within a rectangular channel in order to simulate the motion of the human vocal folds. A pressurized air source provided airflow across the driven model. The model was photographed using a high-speed camera. Detailed flow information was obtained using a hot-wire probe.

A 1.1 Experimental Apparatus

The experimental apparatus consisted of a rectangular channel which was connected to a pressurized air source. The air passed from the source, through the channel, and finally passed by the oscillating vocal folds which were located at the far end of the channel. The channel dimensions were 2.5cm (width) by 3.5 cm (height) by 21cm (length). Static pressure measurements were taken 2.5 cm upstream from the physical model and 2.5 cm downstream from the orifice. Acoustic pressure measurements were not recorded.

Two vibration oscillators were used to drive the motion of the synthetic model. These operated at a frequency of 100 Hz. The motion of the model was captured with a high speed camera capable of taking 3000 images per second. The velocity field 1 mm downstream from the orifice was measured using a small hot wire probe. Figure A.1 provides a schematic diagram of the experimental arrangement. A photograph of the experiment is shown in Figure A.2.

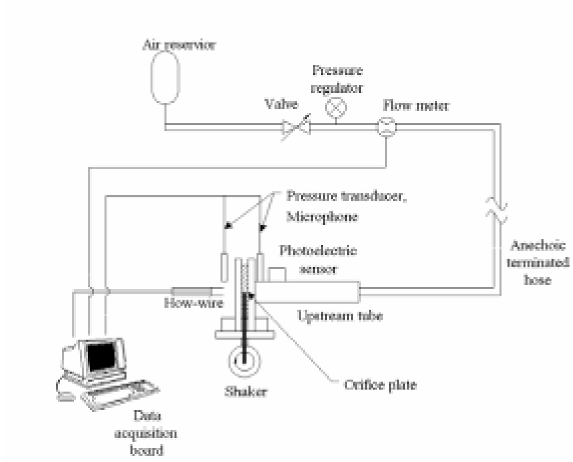

Figure A.1: Schematic diagram of experimental apparatus (from Park et al., in review).

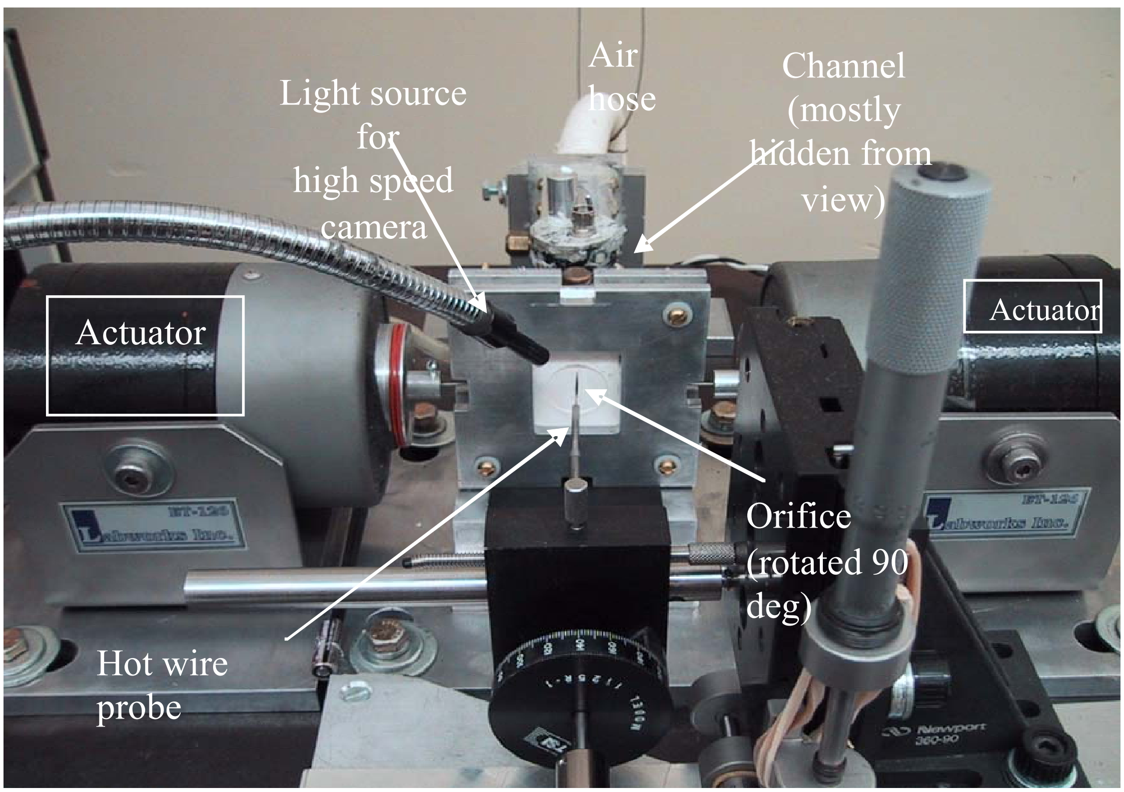

Figure A.2: Photograph of the experimental apparatus.

Images of the physical model taken with the high speed camera at various time steps spanning one period of motion are shown below in Figure A.3. In this figure, symmetry planes are shown in as dashed lines.

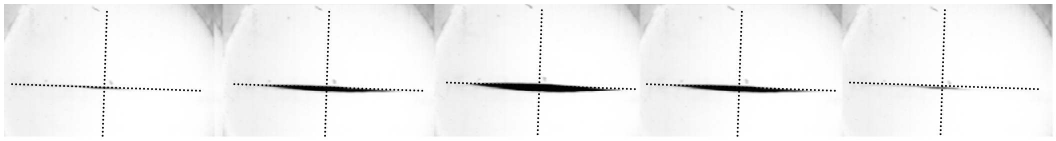

Figure A.3: Images of the driven model over one cycle of oscillation.

Appendix B: Effects of Dimensional Changes on Modal Frequencies

The relative changes of the first five modal frequencies were calculated as a function of the relative changes in each dimension in Section 6.2 The absolute changes in frequency corresponding to Figures 6.2, 6.3, and 6.4 are shown in Figures B.1, B.2, and B.3, respectively. Note that the scale is the same for each figure to facilitate direct comparisons.

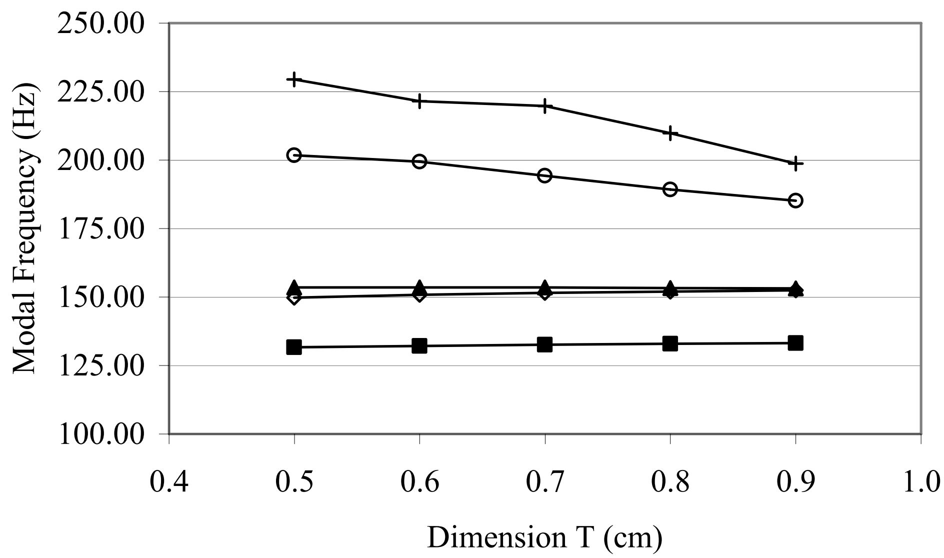

Figure B.1: Modal frequencies as a function of thickness, T.
■ : Mode 1; ◊ : Mode 2; ▲ : Mode 3; ○ : Mode 4; + : Mode 5.

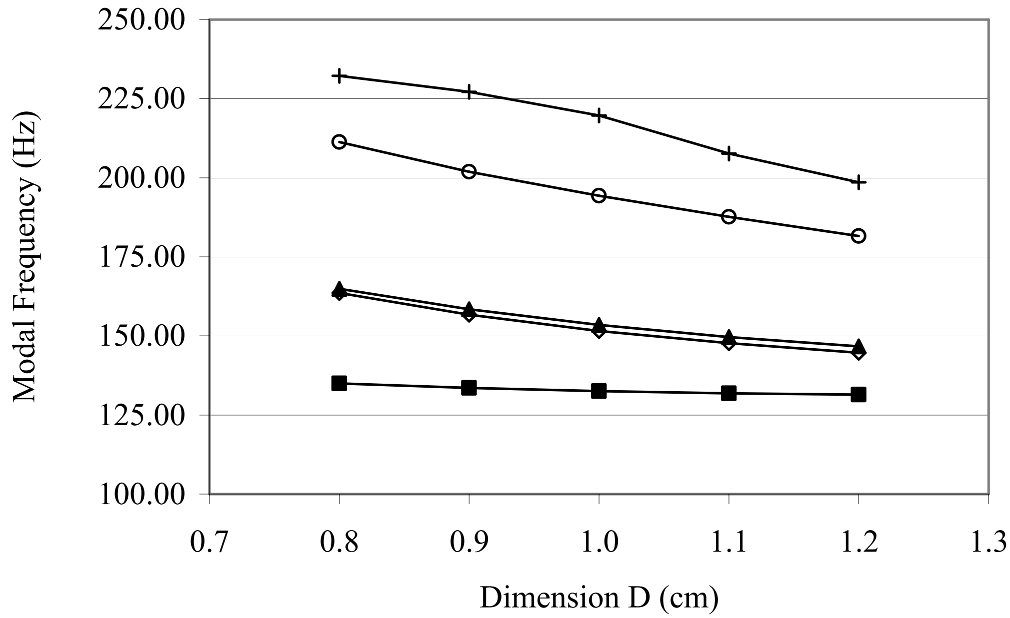

Figure B.2: Modal frequencies as a function of depth, D.
■ : Mode 1; ◊ : Mode 2; ▲ : Mode 3; ○ : Mode 4; + : Mode 5.

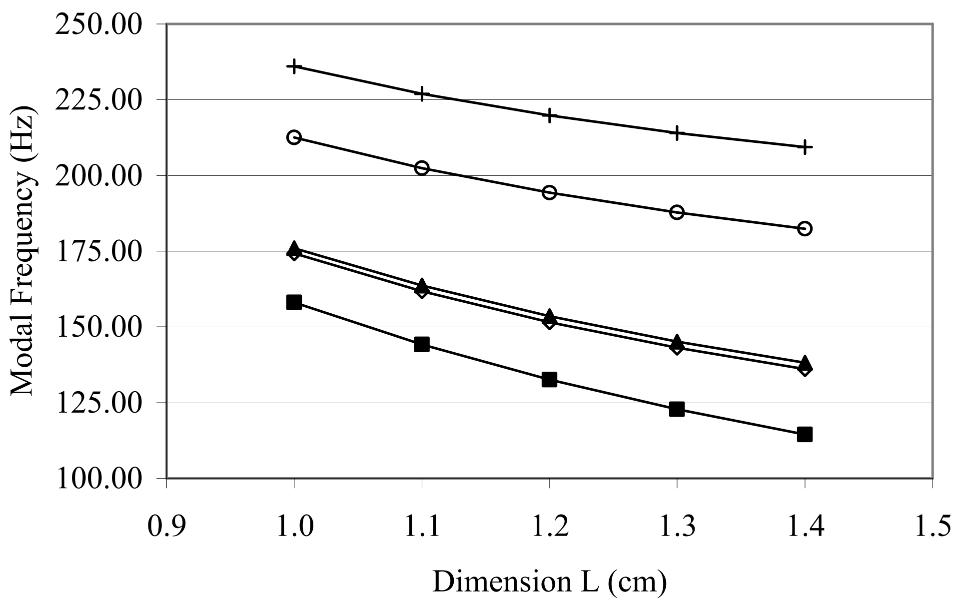

Figure B.3: Modal frequencies as a function of length, L.
■ : Mode 1; ◊ : Mode 2; ▲ : Mode 3; ○ : Mode 4; + : Mode 5.